PROCEEDINGS A

royalsocietypublishing.org/journal/rspa

Review

Cite this article: Fantoni S, Brombal L, Cardarelli P, Baruffaldi F. 2025 Advanced X-ray techniques for research-oriented high-resolution imaging of articular cartilage: a scoping review. *Proc. R. Soc. A* **481**: 20250500. https://doi.org/10.1098/rspa.2025.0500

Received: 9 June 2025
Accepted: 5 November 2025

Subject Areas:
medical physics, biomedical engineering

Keywords:
X-ray imaging, articular cartilage, contrast-enhanced, phase-contrast, diffraction-enhanced imaging, analyser-based imaging, edge-illumination, dark-field

Author for correspondence:
Simone Fantoni
e-mail: simone.fantoni@ior.it

Electronic supplementary material is available online at https://doi.org/10.6084/m9.figshare.c.8174359.

THE ROYAL SOCIETY PUBLISHING

Advanced X-ray techniques for research-oriented high-resolution imaging of articular cartilage: a scoping review

Simone Fantoni[1], Luca Brombal[2,3], Paolo Cardarelli[4] and Fabio Baruffaldi[1]

[1]Medical Technology Laboratory, IRCCS Istituto Ortopedico Rizzoli, via di Barbiano 1/10, Bologna 40136, Italy
[2]Department of Physics, University of Trieste, and [3]Division of Trieste, INFN, via A. Valerio 2, Trieste 34127, Italy
[4]Division of Ferrara, INFN, via G. Saragat 1, Ferrara 44122, Italy

SF, 0000-0003-1459-3356; LB, 0000-0002-4009-8191; PC, 0000-0003-4177-6756; FB, 0000-0001-8784-5652

Articular cartilage (AC) is a musculoskeletal soft tissue renowned for its unique mechanical properties. Understanding both its hierarchical structure and the interplay between its constituents could shed light on the mechanical competence of the tissue. Therefore, rheologic approaches based on high-resolution non-destructive imaging techniques are desired. In this context, X-ray imaging could ideally accomplish this task. Nevertheless, the nature of AC translates into poor contrast using conventional absorption modality. To overcome this limitation, several approaches can be embraced. X-ray visibility of AC can be increased with the use of radiopaque contrast agents (CA). Therefore, further discrimination of structures could be provided by spectral techniques, pivoting on either multi-energy acquisitions or photon-counting technology. Alternatively, phase-contrast (PC) techniques unveil details typically undetected with conventional approaches. Phase-contrast (PC) imaging, based on the intrinsic decrement in the refractive index of the tissue, can be achieved with different configurations and implementations, including distinct X-ray sources and optical elements. In addition, some phase-contrast (PC)

techniques retrieve the small-angle scattering-based dark-field (DF) signal, relatable to sub-pixel structures. This scoping review aims to catalogue the application of these advanced X-ray techniques to AC imaging, following PRISMA guidelines. It discusses their advantages, limitations and includes an overview of rheologic applications to AC.

1. Introduction

Many biomedical imaging techniques allow for non-invasive evaluation of heterogeneous tissues. The osteoarticular tissue represents an excellent case of study, as it features different compositions and structures. Besides its crucial role in clinical routine, imaging of osteoarticular tissues has been extensively investigated in the research frame. In the latter context, the retrieved information is associated with the functional properties of osteochondral tissues. Their degradation, related to pathologies affecting the articulating joints, can be easily depicted with computed tomography (CT) and magnetic resonance imaging (MRI). The roles of CT and MRI have been extensively discussed in the context of clinical diagnostics. However, such discussions are limited to conventional techniques, as diagnostic imaging performed on patients prioritizes minimizing the acquisition times, the possible hazards and the costs. Conversely, biomedical research places more emphasis on different aspects, such as spatial resolution and quantitative accuracy. In this frame, the high-resolution counterpart of CT, the microcomputed tomography (microCT), is preferred.

MicroCT can provide detailed information on microstructures of biological tissues [1], even down to the cellular level, with results comparable to histology [2]. On the other hand, nearly no contrast of soft tissues such as articular cartilage (AC) is achieved, owing to their associated low atomic numbers Z. Consequently, limited information is extracted with conventional X-ray techniques, reducing their potential in assessing AC status. The need for accurate examination of AC and soft tissues, crucial for early disease detection and biomedical analysis, has driven the exploration of alternative X-ray imaging techniques, based on the implementation of non-conventional X-ray sources, detectors, contrast agents (CAs) or their combination.

The aim of the present review is to report on developments achieved in the frame of high-resolution X-ray imaging of AC in recent years, drawing attention to innovative techniques, implemented with different imaging systems.

(a) Articular cartilage (AC)

AC is a connective tissue covering joint surfaces, mainly composed of collagen fibrils (predominantly type II), proteoglycans (PGs) and interstitial fluid. Originating from the deeper zone of the tissue, the collagen fibrils arrange into bundles surging aligned to the AC tissue surface, acquiring the characteristic arcade-like structure. The PGs (i.e. the non-fibrillar component of the extracellular matrix (ECM)) are complex proteins bound with multiple glycosaminoglycans chains, and mainly originate from the pericellular environment of chondrocytes. Their concentration follows a peculiar depth-wise gradient, increasing towards the deep zone of the AC. The chondrocytes distribute inside the tissue in specific sites (i.e. lacunae) and synthetize the main components of ECM. The structure of AC is schematized in figure 1.

The residual negative charge density displayed by glycosaminoglycan chains confers unique properties to the tissue. For instance, the entwined arrangement of PGs in between the collagen bundles generates a spatial outstretch of the ECM, owing to the mutual repulsion of negative charge densities. This effect gives rise to the mechanical pre-tensioning of the AC. Moreover, the charge imbalance draws cations dissolved in the interstitial fluid. The latter results in Donnan osmotic pressure and induces a significant hydration and swelling of the tissue. This phenomenon, together with tissue pre-tensioning and the fibril solid component of the ECM, accounts for the characteristic instantaneous response of AC to any rapid mechanical solicitation. The porosity associated with the packed ECM organization regulates the transient reconfiguration

Abbreviations.

ABI	analyser-based imaging
AC	articular cartilage
CA	contrast agent
CT	computed tomography
CECT	contrast-enhanced computed tomography
DE	dual energy
DF	dark field
DVC	digital volume correlation
ECM	extraCellular matrix
EI	edge illumination
GI	grating interferometry
microCT	microcomputed tomography
MIR	multiple-image radiography
MRI	magnetic resonance imaging
NP	nanoparticle
PBPC	propagation-based phase-contrast
PC	phase contrast
PCD	photon-counting detector
PG	proteoglycan
PMA	phosphomolybdic acid
PTA	phosphotungstic acid
SR	synchrotron radiation
USAXS	ultrasmall-angle X-ray scattering

of interstitial fluid following any mechanical stimulus, until equilibrium is reached [3,4]. In summary, the hierarchical structure and composition of AC translate into near-frictionless and smooth joint motion, provided the integrity of the tissue [3].

The degeneration of the ECM, typically occurring with ageing, after traumas or associated with pathologies (i.e. osteoarthritis), alters both the composition and structure of the AC [5]. Specifically, the fibrillation of collagen bundles, the depletion of PGs and the augmented content of interstitial fluid in the ECM are recognized as hallmarks of AC diseases, along with modifications of underlying subchondral bone [6]. The reduced mechanical performance of AC induces the progressive impairment of joint motion, with severe compromission of an individual's mobility.

In the clinical frame, the early detection of subtle changes in AC could improve the prevention of related musculoskeletal diseases. X-ray imaging methods allow for a detailed depiction of both soft and mineralized tissues at high spatial resolution in restrained acquisition times. For instance, the link between the tissue microstructure and its mechanical response has been investigated to relate the different degradation stages of AC with the tissue functionality. *In situ* testing enables the study of geometrical, morphological and densitometric properties of biological tissues in conjunction with their mechanical properties. In this context, digital volume correlation (DVC) can track down these subtle interrelationships by measuring the full three-dimensional displacement and strain maps under prescribed loading conditions. Nonetheless, the accuracy

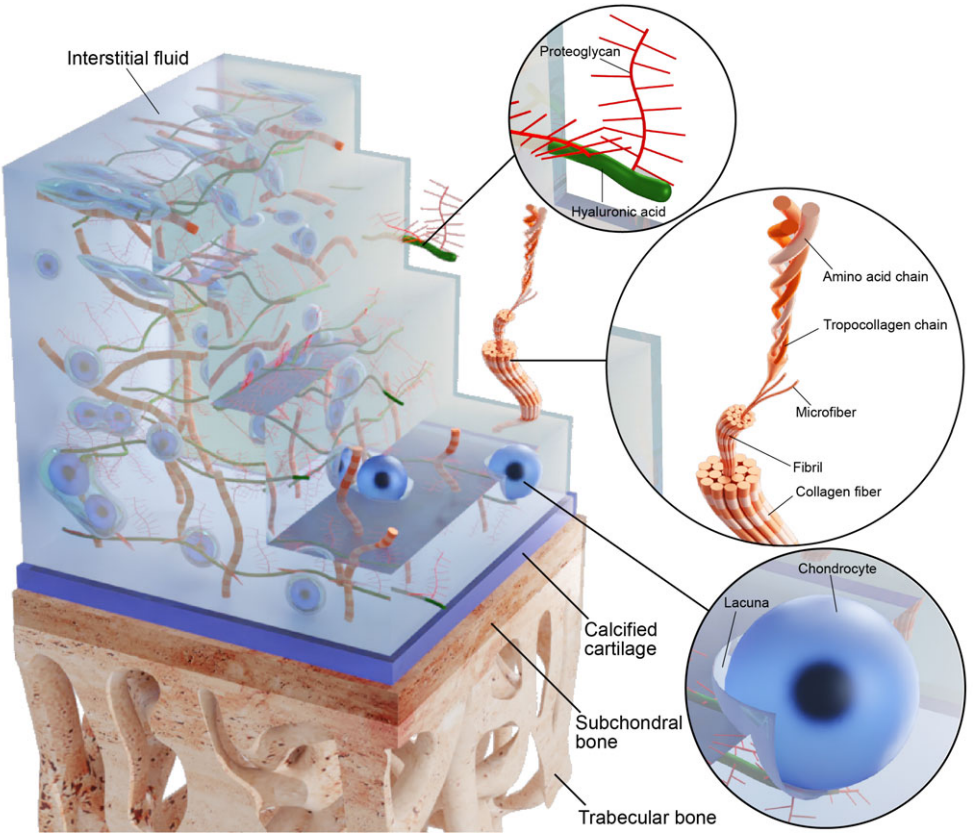

Figure 1. Scheme of AC.

and precision of DVC in measuring displacements strongly depend on the quality of the input images (i.e. signal-to-noise ratio and spatial resolution) [7].

As will be discussed in the review, different mechanisms of image formation yield quantitative information of AC properties, including tissue morphology and composition. The multiple nature of signals (absorption, refraction and scattering of radiation) that can be extracted with advanced X-ray techniques provides meaningful results, as supported by independent methods in the selected literature, and lay the foundations for their use in AC imaging, as introduced hereafter.

2. Advanced X-ray imaging techniques

In general X-ray imaging techniques can give access to three signals, namely, absorption, refraction and scattering phenomena. Absorption-based X-ray methods are easily performed with conventional systems, but result in low contrast of soft tissues owing to their low electron density. The use of high-Z CAs significantly enhances the visibility of inner structures of AC. In this context, to further enhance the discrimination of tissues sharing comparable radiopacity, spectral imaging techniques make use of the specific energy dependence of CA attenuation coefficients. Owing to their spectroscopic capabilities, photon-counting detectors (PCDs) are a crucial implementation for spectral imaging [8]. Refraction-based methods exploit the optical phenomena originating from the shift in the phase of X-ray waves accumulated while traversing the sample. This, in combination with specific geometrical configurations or the insertion of optical elements, allows for the detection of a signal from soft tissue features, generally undetectable with absorption-based approaches. In addition, valuable information on tissue

substructures can be retrieved by assessing the scattering of X-rays in the sample, which can be modelled as a multiple-refraction process at a scale smaller than the system's spatial resolution. Advanced X-ray imaging techniques, allowing for the collection of the different signals previously introduced, can be implemented with laboratory or synchrotron systems. The first category, including conventional microCT scanners, is widely spread thanks to the high availability of commercial systems. Nevertheless, laboratory scanners are mainly devoted to absorption-based modalities, owing to low spatial coherence and limited fluxes. Existing literature reports only a few experiences exploiting microfocus X-ray tubes for phase-contrast (PC) imaging of AC [9]. Synchrotron radiation (SR)-based systems, featuring high fluxes, monochromaticity and high spatial coherence, find applications in retrieving refraction and scattering signals. On the other hand, the limited accessibility to synchrotron facilities hinders their translation to routine practice.

(a) Absorption-based X-ray imaging

(i) Contrast-enhanced computed tomography

Contrast-enhanced CT (CECT) is an absorption-based technique that uses exogenous radiopaque CAs. CAs are compounds including high-*Z* elements, which increase the attenuation coefficient and enhance the contrast of the investigated soft tissue.

First, the selection of CAs depends on the imaging purpose. *In vivo* purposes require non-toxic, FDA-approved CAs [10], whereas the use of heavy metal-based stains [11] and experimental compounds is limited to *ex vivo* and *in vitro* studies, owing to their high toxicity. Among the available CAs, iodine-based formulations have been extensively used to visualize AC (i.e. ioxaglate, iothalame, iohexol, ioversol), as listed in table 1. For research purposes, CA stains generally employed in histology and transmission electron microscopy have also been translated to X-ray imaging protocols.

Second, the effectiveness in enhancing AC X-ray visibility relies upon the properties of the CA molecule, that is, its size, the modality of interaction, and more importantly, its net electric charge. These properties account for the steric hindrance, the reversibility of the contrast enhancement process and the affinity of the CA molecule to the AC, respectively. The molecule size should be tailored to the tissue porosity, to facilitate the permeation in the tissue [110].

The net electronic charge governs the affinity of the CA to components of AC showcasing a charge imbalance. Recalling the composition and structure of AC, only PGs naturally show a net negative fixed charge density.

Otherwise, external alterations in the physiological environment of the ECM (i.e. cleaving of negative charges in acid environment) make collagen fibrils a valuable target for the CA molecules [111]. Clinical CAs are water-soluble small molecules that can be categorized into ionic and non-ionic. The former are preferred to the aims of PG quantitation, thanks to non-covalent electrostatic Coulomb repulsion exerted from negative fixed charge density of PGs. The efficacy of anionic CAs has been demonstrated in various AC models, particularly those involving pathological degeneration. The stronger inverse correlation with PG content justifies the broad adoption of anionic CAs compared to non-ionic CAs [20,38,44,45,47,53,55,65]. In contrast, non-ionic CAs are limited to reveal AC morphology, as their molecules permeate the ECM according to the interstitial fluid distribution, and occasionally with the collagen content [62,82]. The commercial availability of clinical CAs allows their prompt adoption in CECT protocols, aside from adjustments in concentration and osmolality. As a result, numerous works based on clinical ionic CAs extracted quantitative information from AC of different models, including large animals, rodents and humans [22,31,36,42,43,52,58,60,63,64,67,69,71,73–75,78,80,83,87–89,91,92,95–100,103–105,108,109]. Furthemore, anionic CA-enhanced protocols served as a useful tool in monitoring the progression of osteorthritis in several preclinical studies, as confirmed by reference methods such as histology [18,19,21,27,46,49,56,72,84–86,112]. Despite the readiness of clinical CAs, the anti-correlation to PG content is biased by factors in addition to CA accumulation [106]. Moreover, anionic CAs

Table 1. Summary of research papers including X-ray imaging of AC with CECT protocols, ordered from the most to the least recent. For each paper, the corresponding reference is reported, along with the CA used, its net electric charge q, the model for the AC tissue, the size of the specimen S, the voltage V of the X-ray beam, the acquisition time T and the voxel size of the reconstructed volume p. †SR.

ref.	contrast agent	q (e)	model	S (mm)	V	T (min)	p (μm)
[12]	$Na_{0.2}TiO_2$ NPs	NA	bovine	NA	25 keV	NA	9
	$H_{0.3}MoO_3$ NPs	NA			17.5 keV		
[13]	CA4+	+4	equine	Ø 7	70 kVp	NA	36
[14]	Ta_2O_5 NPs	+1	equine	Ø 8.5	150 kVp	NA	40
[15]	PTA	−3	bovine	Ø 4-10	40 kVp	160	3
	Hf-WD POM	−16					
[16]	CA4+	+4	rat	NA	70 kVp	NA	6
[17]	cacodylic acid	NA	rabbit	Ø 2	40 kVp	240	0.65
	$Cl_3H_{18}N_6Ru$	NA					
[18]	ioxaglate	−1	rat	NA	45 kVp	26	16
[19]	iopamidol	−1	murine	NA	55 kVp	20	10.4
			chicken				
[20]	iohexol	0	rabbit	Ø 3.5	40 kVp	NA	18.22
[21]	ioxaglate	−1	equine	NA	90 kVp	2	80
	bismuth NPs	0					
[22]	ioxaglate	−1	rat	NA	55 kVp	NA	8; 12
[23]	CA4+	+4	murine	NA	70 kVp	2.9, 3.5	10
			chicken				
[24]	PTA	−3	guinea pig	NA	60 kVp	NA	10.85
[25]	CA4+	+4	murine	NA	45 kVp	NA	2
			chicken				
[26]	Bi-DOTA	+1	porcine	NA	70 kVp	NA	10.06
	Gd-DOTA	+1					
[27]	ioxaglate	−1	rat	NA	45kVp	27	16
[28]	3,5-diiodo-L-	NA	human	Ø 5	70 kVp	3	10
	tyrosine		murine				
[29]	CA4+	+4	bovine	NA	50 kVp	NA	11.52
[30]	PTA	−3	bovine	3–5	80 kVp	52/181	4.6; 3.4
[31]	ioxaglate	−1	primate	NA	80 kVp	15	90
[32]	CA4+	+4	equine	Ø 7	70 kVp	NA	36
[33]	CA4+	+4	equine	Ø 7	70 kVp	NA	36
[34]	Ta_2O_5 NPs	+13/0	human	NA	70 kVp	NA	36
[35]	CA4+	+4	rabbit	NA	70 kVp	NA	38
[36]	iothalamate	−1	bovine	NA	80 kVp	18	45
[37]	PMA	NA	rat	NA	70 kVp	NA	15

(*Continued*.)

Table 1. (*Continued*.)

ref.	contrast agent	q (e)	model	S (mm)	V	T (min)	p (μm)
[38]	iodixanol	0	primate	NA	NA	NA	NA
[39]	propidium iodide	NA	human	NA	┼12 keV m.	5	2.6
[40]	PTA	−3	human	Ø 3	50 kVp	NA	1.8
[41]	CA4+	+4	bovine	Ø 5	70 kVp	27.9	4
[42]	ioxaglate	−1	goat	75	70 kVp	NA	18
[43]	SiO_2	NA	rat	NA	70 kVp	NA	10
	ioxaglate	−1					
[44]	ioversol	0	mice	Ø 5	55 kVp	NA	57
	iomeron	0	bovine				
[45]	iopimadol	0	rat	NA	47 kVp	NA	21
[46]	ioxaglate	−1	murine	NA	45 kVp	NA	16
[47]	iohexol	0	human	Ø 16.3	84 kVp	17	45
[48]	gadopentetate	−2	human	NA	70 kVp	13	18
	Gd(DTPA)Lys2	+4					
	ioxaglate	−1					
	CA4+	+4					
[49]	ioxaglate	−1	murine	NA	70 kVp	NA	6
[50]	CA4+	+4	human	NA	NA	NA	100
[51]	PTA	−3	human	Ø 4	80 kVp	120	3.0
					45 kVp		3.2
[52]	ioxaglate	−1	rat	NA	45 kVp	NA	14.8
[53]	iopimadol	0	bovine	Ø 10	70 kVp	NA	16
			porcine				
[54]	CA4+	+4	equine	Ø 7	70 kVp	NA	36
[55]	iohexol	0	human	NA	68 kVp	18	61
[56]	ioxaglate	−1	rat	NA	45 kVp	27	16
[57]	PTA	−3	murine	NA	90 kVp	NA	2.5
[58]	ioxaglate	−1	human	NA	70 kVp	40	36
[59]	CA4+	+4	human	NA	120 kVp	NA	41
[60]	ioxaglate	−1	rat	NA	45 kVp	26	16
[61]	CA4+	+4	human	NA	120 kVp	NA	41
[62]	ioxaglate	−1	equine	Ø 6	66 kVp	NA	10
	iodixanol	0					
[63]	CA4+	+4	bovine	Ø 7	70 kVp	NA	36
	ioxaglate	−1	rat				
	iodixanol	0					
[64]	Bi_2O_3	NA	bovine	Ø 7	100 kVp	NA	15.98
	ioxaglate	−1					

(*Continued*.)

Table 1. (*Continued*.)

ref.	contrast agent	*q* (e)	model	*S* (mm)	*V*	*T* (min)	*p* (μm)
[65]	meglumine diatrizoate	−1	rat	NA	45 kVp	NA	16
[66]	PTA	−3	human	Ø 4	80 kVp	100	3
[67]	CA4+	+4	murine	NA	45 kVp	NA	3
	ioxaglate	−1					
[68]	uranyl acetate	NA	human	NA	70 kVp	NA	13; 2.94
	lanthanide solution	NA	rat				
	IKI	NA					
	PTA	−3					
	iopamidol	0					
[69]	PTA	−3	bovine	Ø 4.8	40 kVp	8	17.4
	ioxaglate	−1					
[70]	CA4+	+4	human	Ø 2	45 kVp	122	3.2
[71]	ioxaglate	−1	rat	NA	90 kVp	3	21
[72]	ioxaglate	−1	rat	NA	45 kVp	24.7	16
[73]	ioxaglate	−1	human	NA	95 kVp	30-90	35
[74]	SiO_2	NA	rabbit	NA	70 kVp	NA	18
	ioxaglate	−1					
[75]	ioxaglate	−1	canine	NA	40 kVp	NA	13.4
[76]	CA4+	+4	murine	NA	70 kVp	NA	2; 6
[77]	CA2+	+2	bovine	Ø 6	100 kVp	NA	25
[78]	ioxaglate	−1	rabbit	NA	45 kVp	NA	20
[79]	PTA	−3	equine	Ø 6	80 kVp	32	8.7
	PMA	NA	human	Ø 4.6	80 kVp	135	3.2
[80]	meglumine diatrizoate	−1	human	Ø 12	50 kVp	11	18
[81]	CA4+	+4	human	NA	70 kVp	NA	36
	ioxaglate	−1					
[82]	meglumine diatrizoate	−1	bovine	4	50 kVp	NA	18
[83]	ioxaglate	−1	rat	NA	55 kVp	42	10
[84]	ioxaglate	−1	rat	NA	55 kVp	42	10
[85]	ioxaglate	−1	rat	NA	65 kVp	NA	18
[86]	ioxaglate	−1	rat	NA	65 kVp	NA	18
[87]	ioxaglate	−1	human	NA	70 kVp	36	18
			murine				
[88]	ioxaglate	−1	murine	NA	60 kVp	20	2
[89]	ioxaglate	−1	rat	NA	60 kVp	NA	20
[90]	Ta_2O_5 NPs	NA	human	NA	50 kVp	NA	6; 36; 100
	ioxaglate	−1	rat				
[91]	iothalamate	−1	bovine	NA	58 kVp	NA	70; 100

(*Continued*.)

Table 1. (*Continued*.)

ref.	contrast agent	*q* (e)	model	*S* (mm)	*V*	*T* (min)	*p* (μm)
[17]	PTA	−3	murine	NA	50 kVp	NA	5
[92]	ioxaglate	−1	rat	NA	45 kVp	NA	16
[93]	CA4+	+4	bovine	Ø 7	70 kVp	NA	36
	ioxaglate	−1	rabbit		50 kVp		100
[94]	CA4+	+4	bovine	Ø 7	70 kVp	NA	36
[95]	meglumine diatrizoate	−1	rat	NA	70 kVp	NA	18
[96]	ioxaglate	−1	human	NA	55 kVp	360-600	35
[97]	ioxaglate	−1	murine	NA	45 kVp	NA	6
[98]	ioxaglate	−1	murine	NA	60 kVp	20	2
[99]	ioxaglate	−1	rat	NA	55 kVp	NA	35
[100]	ioxaglate	−1	human	NA	55 kVp	360–600	35
[101]	CA4+	+4	bovine	Ø 7	70 kVp	NA	36
	ioxaglate	−1					
	gadopentetate	−2					
[102]	CA4+	+4	bovine	Ø 7	NA	NA	70; 36
	CA1+	+1	rabbit				
	iothalamate	−1					
[103]	ioxaglate	−1	rat	NA	45 kVp	NA	12; 16
[104]	iothalamate	−1	bovine	Ø 7	NA	NA	70; 100
[105]	ioxaglate	−1	rat	NA	45 kVp	NA	12
[106]	gadopentetate	−2	human	NA	60 kVp	NA	41
[107]	CA1+	+1	rabbit	NA	45 kVp	NA	30
	CA2+	+2					
	CA4+	+4					
	iothalamate	−1					
	ioxaglate	−1					
[108]	ioxaglate	−1	rat	NA	55 kVp	15	35
[109]	ioxaglate	−1	bovine	Ø 4	45 kVp	NA	21
			rabbit				

reasonably enhance the tissue discernability at the cost of conspicuous CA concentrations, with further concerns related to beam-hardening effects [55].

In the realm of experimental CAs, the formulation of novel molecules focused on more advantageous mechanisms of interactions with AC components. The first experimental cationic CAs [107] offered higher iodine content per molecule and electrostatic attraction to PGs, yielding superior discrimination of AC. Further correlations with AC composition were confirmed with reference methods (i.e. histology and biochemical assay), at significantly lower concentrations compared to clinical anionic molecules [16,23,25,29,54,70,76,77,81,93,101,102] (see figure 2a). Furthermore, mechanical tests confirmed the intertwined relationship between the attenuation of cationic CA and the mechanical behaviour of AC, considering the tissue's elastic, frictional and equilibrium properties [13,32,33,35,41,48,50,59,61,63,81,94].

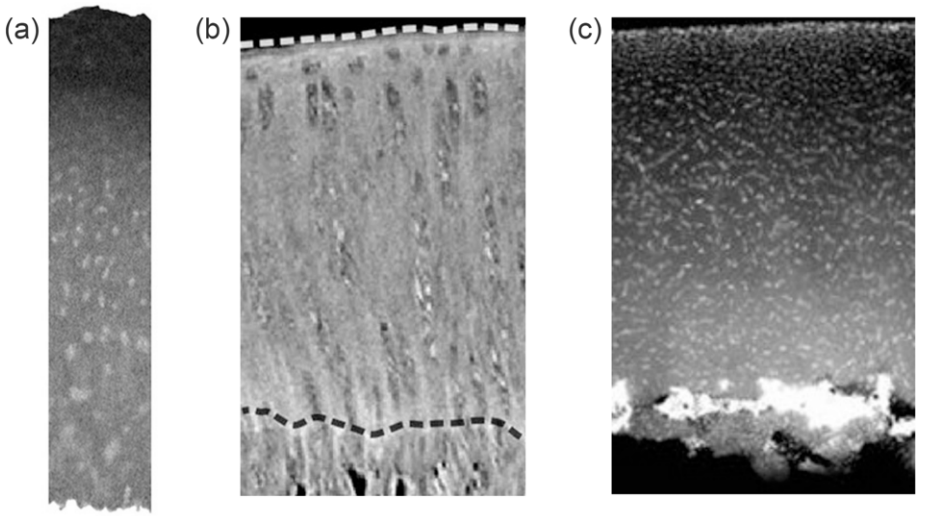

Figure 2. (a) Section from contrast-enhanced microCT of human AC, following the immersion in CA4+ solution (3.2 µm pixel size, commercial microCT scanner). Along with the characteristic gradient of radiopacity increasing towards the deep layer of AC, spots with augmented signal are recognizable as chondrocytes' lacunae. Image adapted from the work of Karhula *et al.* [70], published under Creative Commons license (CC BY 4.0). (b) Section from contrast-enhanced microCT of rabbit AC, following the immersion in solution of hexaammineruthenium(III) chloride and cacodylic acid (0.65 µm pixel size, commercial microCT scanner). The proposed protocol aimed to investigate the collagen fibre orientation in a osteoarthritic AC model (dashed white line and dashed black line mark tissue surface and tidemark, respectively). Image adapted from the work of Ojanen *et al.* [113], published under Creative Commons license (CC BY 4.0). (c) Section from contrast-enhanced microCT of human AC, following the immersion in propidium iodide (2.6 µm pixel size, SR-microCT). The direct binding of the selected CA to DNA in chondrocytes allowed the punctual depiction of the cellular pattern, enabling the quantification of chondrocytes' distribution even inside each lacuna. Image adapted from the work of Danalache *et al.* [39], published under Creative Commons license (CC BY 4.0).

Besides iodine, other radiopaque candidates have been selected for AC visualization. Gadolinium is a chemical element of lanthanide series, and enters the composition of MRI CAs, owing to its paramagnetic properties. In the clinical formulations, gadolinium-based CAs are predominantly non-ionic or anionic, and are employed as well as the iodine-based CAs, to signal water content and PG distribution [48,106]. Owing to its different K-edge energy (50.2 keV) with respect to iodine (33.2 keV), gadolinium-based CAs can be used simultaneously along with iodine-based CAs in dual energy (DE) and multi-energy protocols [114–120]. In the wake of novel formulations, a cationic molecule containing bismuth yielded greater correlations to reference methods for assessing PGs, compared to analogous molecules [26].

Laboratory stains, usually employed in histology and transmission electron microscopy, offer a valid alternative to clinical CAs. For instance, polyoxometalates such as phosphotungstic acid (PTA) e phosphomolybdic acid (PMA) considerably increase the X-ray visibility of the exposed soft tissue [11]. Nevertheless, different binding mechanisms oblige fixation and dehydration of the tissue, leading ot irreversible alterations of its properties. While effective for collagen quantification [17,30,37,40,51,57,68,79,113] (see figure 2b), imaging protocols based on polyoxometalates imply alterations of the AC incompatible to mechanical testing [15]. Only in recent times, the adoption of physiological environments has limited the forthcoming modifications of AC properties, following the exposure to such stains [24].

Further efforts to enhance the imaging outcome of existing CAs include functionalizing ioxaglate to specifically bind to PG [112] or tyrosine (an amino acid naturally containing iodine) to type-II collagen of ECM [28]. In recent years, increasing attention has been addressed to nanoparticles (NPs) owing to their small size (1–1000 nm) and tunable physicochemical

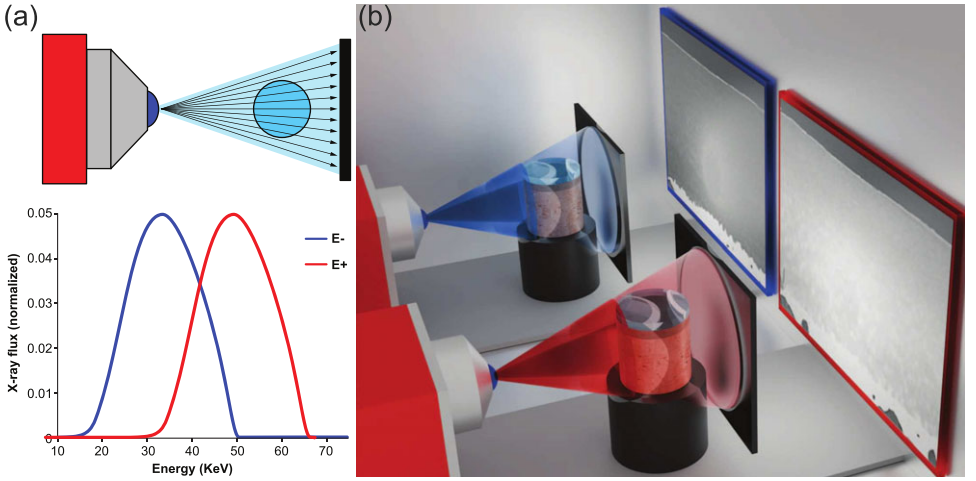

Figure 3. (a) Scheme of DE technique. The procedure includes two distinct X-ray exposures, each at a different beam energy. The low-energy and high-energy components serve as input for decomposition algorithms, to deliver two material maps. (b) Reconstructed section from low-energy $E-$ and high-energy $E+$ binned photons is reported on blue and red screen, respectively. In the low-energy and high-energy screens are reported sections from reconstructed volume of AC, following the immersion in a gadoteridol/CA4+ mixture. In particular, the contrast in low- and high- energy sections is due mainly to gadoteridol and CA4+, respectively. Images on screens of panel (b) adapted from the work of Honkanen *et al.* [118], published under Creative Commons license (CC BY 4.0).

properties, including shape, hindrance, and composition [90,121]. For instance, tantalum-based NPs enable the quantitation of PG [14,34] or ensure the detection of defects in the tissue [12].

In existing literature, only few studies addressed CECT on chondrocyte imaging, owing to the demanding spatial resolution. Rather than the cells themselves, the imaging of lacunae (namely, the cavities in ECM enclosing one or more chondrocytes, with typical size of 10 µm [122]) allows for more relaxed imaging protocols, carried out with nano-focus X-ray tubes. Following the contrast enhancement, lacunae were reportedly depicted as focalized sites featuring a radiopacity different from the surrounding ECM [66,70]. Nevertheless, laboratory-based systems equipped with X-ray tubes require long acquisition times, raising concerns about the stability of the sample over time. Such issue can be overcome with SR. For instance, the high monochromatic flux significantly lowers the scan time and ensures spatial resolution down the cellular level [39] (see figure 2c).

(ii) Dual-energy (DE) imaging

DE and, more in general, multi-energy imaging is based on several acquisitions taken at different X-ray beam energies. This method can provide information on sample composition, if unknown, or conversely, allows reconstructing the density distribution of certain elements, provided that the composition is known *a priori* [123]. DE imaging is particularly useful when CAs or naturally occurring high-Z materials are present within the sample. By making use of attenuation properties specific to the material of interest, such as the K-edge, it is possible to discriminate structures containing the high-Z element, even though they have an overall attenuation similar to the surrounding features [124]. This is achieved through dedicated material decomposition algorithms, which, having as input two (or more) attenuation images at different energies, provide density maps of two (or more) materials. A scheme of DE technique is reported in figure 3. The ideal conditions for DE imaging are obtained using monochromatic beams, as in the case of SR [125,126] or laser-driven radiation sources [127]. In this case, the material decomposition

Table 2. Summary of research papers including X-ray imaging of AC with DE protocols, ordered from the most to the least recent. For each paper, the corresponding reference is reported, along with the CA used, its net electric charge *q*, the model for the AC tissue, the size of the specimen, the source type, the voltage *V* or associated energy *E* of the X-ray beam (m., monochromatic), the acquisition time *T* and the voxel size of the reconstructed volume *p*.

ref.	contrast agent	*q* (e)	model	*S* (mm)	source	*V*/*E*	*T* (min)	*p* (μm)
[120]	CA4+	+4	equine	NA	X-ray tube	50/90 kVp	2.6	59
	gadoteridol	0						
[119]	CA4+	+4	human	Ø 8	X-ray tube	50/90 kVp	NA	40
	gadoteridol	0		Ø 8				
[117]	CA4+	+4	bovine	Ø 7	synchrotron	32/34 keV m.	2.15	6.5
	gadoteridol	0						
	Bi-NPs	0						
[118]	CA4+	+4	human	Ø 8	synchrotron	32/34 keV m.	2.15	6.5
	gadoteridol	0						
[116]	CA4+	+4	human	Ø 8	X-ray tube	50/90 kVp	NA	40
	gadoteridol	0						
[115]	CA4+	+4	bovine	Ø 4	synchrotron	25/37 keV	2.1	6.5
	gadoteridol	+4						
[114]	CA4+	+4	human	Ø 8	X-ray tube	50/100 kVp	18/10	25
	gadoteridol	0						

problem can be solved exactly, owing to the absence of beam-hardening, which is commonly encountered when polychromatic spectra are used.

In the context of AC X-ray imaging, the DE technique offers its potential in discerning two or more CAs, when used simultaneously. In particular, radiopaque CAs with different attenuation signatures (i.e. K-edge energies) are selected to track single AC components (see table 2). The X-ray energies are carefully chosen to enclose the attenuation discontinuities of the selected CAs separately. By applying material decomposition algorithms to the DE dataset, the density maps of the elements of interest are obtained [124]. Such protocols were applied to understand the various factors influencing CA diffusion in AC [114,116,119,120]. Specifically, iodine accounted for the PG content, owing to the electrostatic repulsion between the anionic CA and the negative fixed charge density of glycosaminoglycans. In contrast, gadolinium CA tracked the water content.

The concurrent determination of ionic and non-ionic partitions improved the correlation between the PG-related iodine distribution and AC mechanical properties [114,115,117,119, 128,129]. DE methods can be further implemented with SR. The monochromaticity and high fluxes of the generated beam ensure improved image quality and reduced scan times [115,117,118]. Nevertheless, the material decomposition comes with the increase of radiation dose deposited to the sample, proportional to the number of X-ray exposures (i.e. number of X-ray energies) and the exposure time. On the other hand, the development of novel detectors has enabled the simultaneous measurement of transmitted X-ray photons in multiple energy windows, by using one single polychromatic X-ray exposure.

(iii) Detector-based spectral imaging

PCDs discriminate the incoming photons depending on their energy, and have recently found applications in several imaging fields [130]. Photon-counting technology is based on the direct conversion of incoming photons by semiconductors sensors and the following discrimination of the signal at the pixel level. Unlike scintillator elements in energy-integrating detectors,

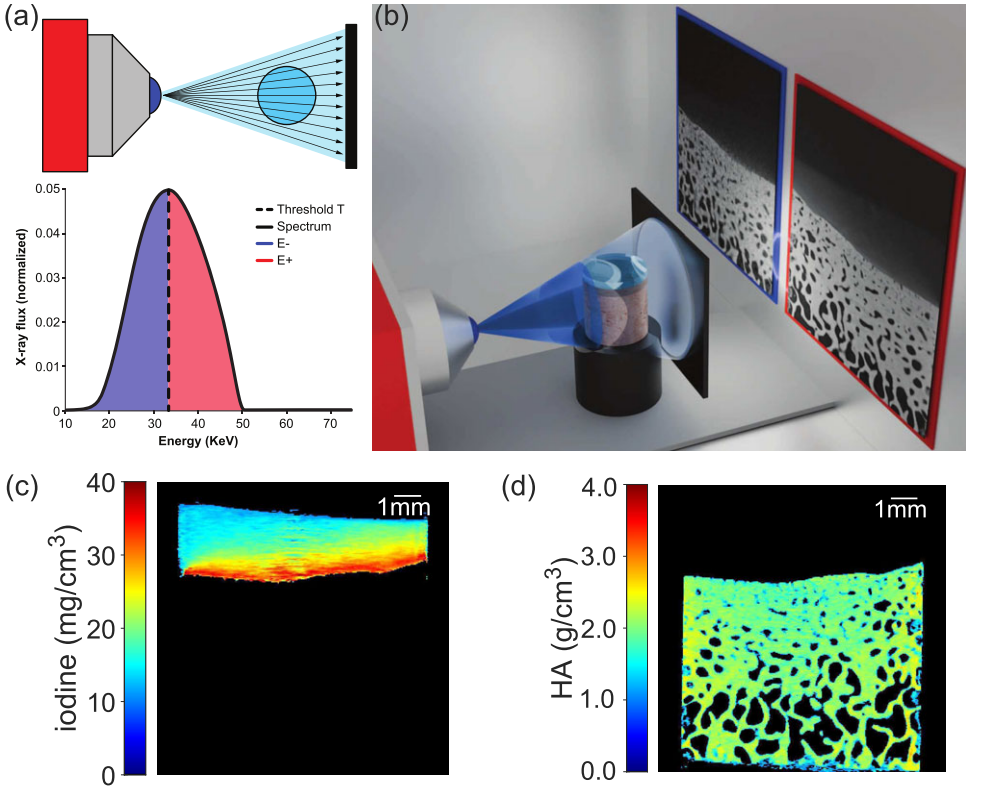

Figure 4. (a) Scheme of spectral imaging technique. The procedure includes a single X-ray exposure. The discrimination occurs on-chip, following the selection of an energy threshold. According to the latter, photons are binned in low-energy and high-energy components. Analogously to DE technique, both components are required for decomposition algorithms to provide two material maps. (b) Reconstructed section from low-energy $E-$ and high-energy $E+$ binned photons of a bovine osteochondral sample is reported on blue and red screen, respectively. (c,d) Section of density maps, as a result of the decomposition algorithm. (c) Iodine density map accounting for iodine-based CA4+ diffused in AC. (d) Hydroxyapatite (HA) density, accounting for calcium-rich bone tissue. Images in panels (b–d) adapted from the work of Fantoni *et al.* [133], published under Creative Commons license (CC BY 4.0).

which achieve X-ray conversion into visible light, semiconductors enable the direct conversion of incoming photons into electric signal, with an intensity proportional to the energy deposited by each interacting photon to the sensitive region of the detector [131]. Within each pixel of a PCD, this signal is discriminated based on one (or more) energy-calibrated threshold(s). If multiple energy thresholds are available, photons can be detected and grouped over multiple energy intervals (or bins). In this way, a single X-ray exposure yields multiple attenuation maps—as many as the energy bins defined by the thresholds. The application of decomposition algorithms selectively enhances or eliminates structures in the sample, similarly to DE imaging [132]. The principles of spectral imaging are summarized schematically in figure 4. Unlike DE methods, polychromatic X-ray beams are employed, and no specific constraints on X-ray spectrum are required. Therefore, the implementation of PCDs is suitable for clinical [134] and laboratory [135] X-ray systems.

Detector-based spectral imaging yields promising results in terms of AC discernability, although the spatial resolution of clinical scanners remains limited [136,137]. This issue is partially solved by laboratory-based spectral systems equipped with small pixel (less than 100 μm) PCDs, where the spatial resolution has been significantly improved. Previous experiments verified the suitability of spectral imaging *ex vivo* and *in vitro* on human specimens, exposed to several CAs

Table 3. Summary of research papers including X-ray imaging of AC with PCD-based spectral protocols, ordered from the most to the least recent. For each paper, the corresponding reference is reported, along with the CA used, its net electric charge q, the model for the AC tissue, the size of the specimen S, the PCD model, the voltage V of the X-ray beam, the acquisition time T and the voxel size of the reconstructed volume p.

ref.	contrast agent	q (e)	model	S (mm)	PCD	V	T (min)	p (μm)
[139]	Ta_2O_5 NPs	+4	equine	Ø 8.5	Xcounter	150 kVp	NA	68
	iodixanol	0			XC-Flite FX15	120 kVp		
[133]	CA4+	+4	bovine	Ø 10	Pixirad1-PixielII	50 kVp	120	34
[129]	CA4+	+4	human	Ø 8	0.75mm CdTe	100 kVp	NA	87
	gadoteridol	0			100um pixel size			
[141]	ioxaglate	−1	bovine	Ø 8	2 mm CdTe	80/120 kVp	NA	110
	gadobenate	−3	human		Medipix3RX			
[140]	ioxaglate	−1	human	25	2 mm CdTe	80 kVp	NA	73
					Medipix3RX			

[129,138,139]. Alternatively, other works exploited a single CA but aimed to distinguish between the contrast-enhanced AC and the underlying bone tissue [133,140,141] (see figure 4c,d), even down to the smallest pixel size reported for a spectral imaging system, namely, 34 μm (see table 3).

(b) Refraction-based X-ray imaging techniques: phase-contrast (PC)

PC imaging exploits the phase shift of X-rays interacting with the sample. PC rises from interference phenomena involving the wavefront distorted by the sample [142]. The modulation of the wavefront can be described by the phase shift accumulated by the incoming X-ray wave while traversing the sample, which is proportional to the decrement from unity of the real part δ of the complex refractive index. Conversely, it can be demonstrated that X-ray attenuation, which is used in conventional X-ray imaging, is proportional to the imaginary part β of the complex refractive index ($n = 1 - i\beta - \delta$). In the case of soft tissues and energies used in conventional radiology (10–100 keV), PC is advantageous as δ is two to three orders of magnitude larger than β, allowing to highlight internal structures related to subtle fluctuations of density or interfaces without using exogenous CAs [143]. The sample-induced phase-shift can be related to refraction effects where local modifications to the wave vector can be described, in a simplified ray-tracing model, as small-angle deviations (order of microradians) of the impinging X-rays [144]. As the X-ray wave phase cannot be directly measured with imaging detectors, several PC techniques have been developed to transform the phase shift into detectable intensity modulations. Some of these techniques pose strict requirements on the X-ray beam coherence (i.e. monochromaticity and small focal spot size), and are therefore primarily implemented within SR facilities [145–147]. More recently, alternative PC set-ups with relaxed coherence requirements have been introduced, therefore making PC imaging accessible within laboratory settings [148,149]. In the following subsections the image formation principles of the most widely used PC techniques are illustrated.

(i) Propagation-based phase-contrast

Propagation-based PC (PBPC) imaging is the simplest PC technique to implement, as no optical element is required [150]. PBPC requires increasing sample-to-detector distance to generate a phase shift-induced interference pattern on the detector. This is generally visible as a couple of dark/bright fringes corresponding to interfaces between materials with different refractive indices, and it is referred to as the edge-enhancement effect.

Table 4. Summary of research papers including X-ray imaging of AC with PBPC protocols, ordered from the most to the least recent. For each paper, the corresponding reference is reported, along with the model for the AC tissue, the size of the specimen *S*, the source type, the voltage *V* or associated energy *E* of the X-ray beam (m., monochromatic; p., polychromatic; p.b., pink beam), the acquisition time *T*, the voxel size of the reconstructed volume *p* and the object-to-distance ODD.

ref.	model	*S* (mm)	source	*V*/*E*	*T* (min)	*p* (μm)	ODD (cm)
[152]	bovine	Ø 4	synchrotron	21 keV m.	0.08–0.66	2.75	40
[153]	bovine	Ø 4-6	synchrotron	17 keV m.	66	3.5	250
[154]	human	Ø 7	synchrotron	60keV m.	NA	6.1	1100
				55 keV p.		0.7	120
				17 keV m.		0.325–0.1	10
[155]	murine	NA	synchrotron	52 keV m.	8	6.1; 6.06	1100
		NA	X-ray tube	60 kVp	NA		
[156]	bovine	Ø 3-4	X-ray tube	40 kVp	NA	2.02–2.56	NA
[157]	human	Ø 7	synchrotron	26.1 keV p.b.	NA	5.1	500
[158]	murine	NA	synchrotron	12-25 keV p.b.	1.1–7.3	0.8–1.6	NA
				19 keV m.	37.5	1.1	NA
[159]	human	NA	synchrotron	60 keV m.	1.5	46	700
[160]	murine	NA	synchrotron	NA	NA	NA	NA
[161]	rabbit	NA	synchrotron	5–18 keV p.	NA	10	NA
[162]	murine	NA	synchrotron	14 keV m.	NA	3.7	NA
[163]	human	NA	synchrotron	60 keV m.	90	46	700
[164]	bovine	Ø 2	synchrotron	14 keV m.	60–180	1.752	0.5–30.0
[165]	murine	NA	X-ray tube	80 kVp	30	9/6.6	32.2
[166]	horse	0.2-1	X-ray tube	70 kVp	NA	13	NA
	human			11.2 keV m.		15	NA
[167]	murine	NA	synchrotron	7–14 keV p.	NA	1.48	5
[2]	bovine	NA	synchrotron	10–15 keV m.	40	1.6	15
[168]	human	20	synchrotron	30 keV m.	NA	NA	NA

Since the spatial coherence of the X-ray beam is crucial for PBPC [150], this technique can be implemented with SR, laser-driven systems, or high-end microfocus X-ray tubes [151] (see table 4). A scheme of image formation via PBPC is displayed in figure 5. Images featuring the edge-enhancement effect can be further processed with phase-retrieval algorithms, which enable the recovery of the phase-shift information [169] and enhance the signal-to-noise ratio, hence the visibility, of soft tissue structures [169,170].

In the literature, PBPC has been demonstrated as a suitable imaging technique, not only in visualizing AC without the need for CA, but also in unveiling the most subtle structures. The ability to clearly distinguish AC was confirmed by studies based on planar [166–168] and tomosynthesis approaches [160,161]. Reduced thickness and augmented roughness of the AC surface have been recognized as hallmarks of AC degeneration in diseased models [159,160]. The transfer of PBPC to tomographic acquisitions confirmed these observations [155,162,165]. Boosting the resolution of the acquisition system down to few μm, the sensitivity of PBPC technique to cellular pattern was further enhanced with specific CAs and validated by independent methods such as histology [9,171,172] (see table 5). Besides the coherence of

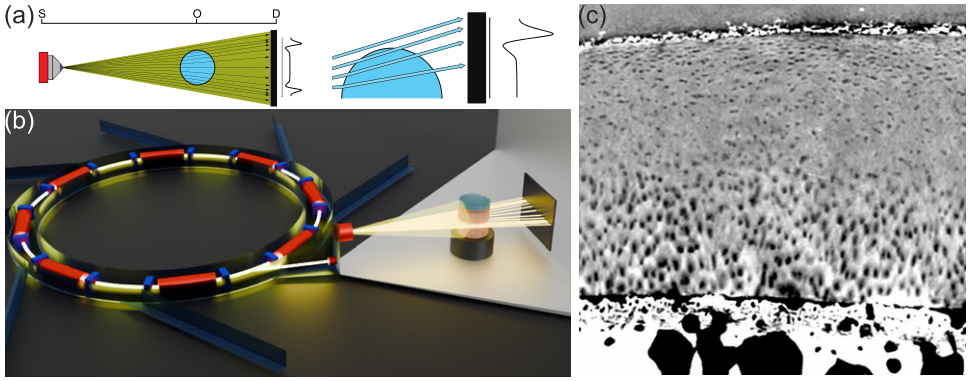

Figure 5. (a) Scheme of PBPC. Unlike absorption modalities, PBPC bases its mechanism on the distance between the sample and the detector. In particular, such distance is selected to produce the edge-enhancement, originating from interfaces between different materials. (b) Three-dimensional rendering of a typical PBPC set-up. The edge-enhancement requires a high degree of spatial coherence (i.e. SR). (c) Section from PBPC volume of healthy human AC. Besides the interface AC/air on the top, darker spots in the tissue, attributable to chondrocytes' lacunae, are clearly recognizable. Image adapted from the work of Horng *et al.* [154], published under Creative Commons license (CC BY 4.0).

Table 5. Summary of research papers including X-ray imaging of AC with contrast-enhanced PBPC protocols, ordered from the most to the least recent. For each paper, the corresponding reference is reported, along with the CA and its charge q, the model for the AC tissue, the size of the specimen S, the source type, the voltage V of the X-ray beam, the acquisition time T, the voxel size of the reconstructed volume p and the object-to-distance ODD.

ref.	contrast agent	q (e)	model	S (mm)	V	T (min)	s (μm)	ODD (cm)
[173]	RHT	NA	murine	NA	NA	NA	NA	NA
	cacodylic acid	NA						
	OsO_4	NA						
[172]	PTA	−3	ovine	Ø 10	80 kVp	NA	4.5	9.5
					60 kVp	NA	10.2	17.2
[9]	PTA	−3	bovine	Ø 3	40 kVp	NA	1.97–2.85	4.0–55.8
[174]	PTA	−3	murine	NA	NA	NA	NA	NA
[175]	OsO_4	NA	murine	NA	NA	NA	NA	NA
			equine					
[171]	OsO_4	NA	murine	NA	40–80 kVp	65–1067	0.54–10	2.5–7.5
[176]	OsO_4	NA	murine	NA	40 kVp	NA	4	7.5
[177]	RHT	NA	murine	NA	NA	NA	NA	NA
	cacodylic acid	NA						
	OsO_4	NA						

the beam, the object-to-detector distance is crucial for the visualization of lacunae, that is, the interfaces between the inner chondrocytes from the surrounding ECM.

Larger sample-to-detector distances and higher beam energies of the X-ray beam were demonstrated to be beneficial for the optimal visualization of structural details [2]. Note that the proposed imaging protocol also distinguishes chondrocyte from the surrounding lacunae, as confirmed by scanning electron microscope images [2,164]. Horng *et al.* further pushed the

evaluation of healthy and diseased AC down at sub-cellular level, even highlighting the cellular nucleus and bundles of collagen fibres with the highest spatial resolution of 0.1 µm [154] (see figure 5c).

Other studies, rather than focusing on cellular-scale details, analysed the morphology of AC on larger scales. The acquisition of whole cadaveric human joints yielded not only the delineation of several soft tissues, but also the differentiation of AC layers. The latter feature was observed to vary substantially from healthy to osteoarthritic AC. The authors speculated that the loss of chondrocytes associated to the pathology could imply a variation in the electron density associated with the retrieved signal [163].

The quantitative analysis was also carried out with the application of Paganin phase-retrieval, assigning different grey level windows, according to the heterogeneous arrangement of components in the ECM [153,154,157]. Unless more complex acquisition schemes are implemented, such as in the case of holotomography [178], a quantitatively accurate phase-retrieval requires strict assumptions on sample composition [179]. Alternatively, the phase information can be accessed with different imaging configurations, making use of optical elements in the imaging set-up. These approaches are discussed in the following subsections.

(ii) Analyser-based imaging

Analyser-based imaging (ABI) makes use of a perfect crystal, referred to as the analyser, set between the object and the detector [180–182], and requires a monochromatic and laminar X-ray beam. The analyser crystal acts as an angular filter of the incoming X-ray beam. When the analyser crystal is set to an angle that satisfies Bragg's condition with respect to the incoming beam, X-rays are transmitted (i.e. diffracted). The transmission efficiency decreases as the analyser is rotated away from Bragg's condition. The curve describing the X-ray transmission as a function of the analyser crystal's angle is called the rocking curve [180].

As the angular acceptance of the rocking curve is in the order of some microradians, the analyser crystal allows the translation of X-ray refraction into intensity modulation with high sensitivity. By acquiring images at different angles of the analyser crystal, that is, different points on the rocking curve, both attenuation and (differential) phase signal can be obtained via dedicated algorithms. In addition, if at least three images are acquired in different positions of the rocking curve, ABI allows the extraction of the scattering or dark-field (DF) signal, hence giving access to structures below the system's spatial resolution [181–183]. While ABI is usually associated with high image quality and quantitative accuracy, its use is mostly limited within SR facilities owing to the need for intense monochromatic laminar beams. The mechanism behind the image formation of ABI is outlined in figure 6.

The potential of ABI for AC depiction was explored in the first 2000s at different synchrotron facilities. Although the first images were radiographies impressed on radiographic film, they provided robust results in terms of discernability of soft tissues [185–190]. The positioning of the analyser crystal was crucial for AC visualization. Depending on the analyser tilting, only those photons emerging from the sample within the angular acceptance range of the rocking curve (order of a few µrad) reach the image plane. Therefore, different structures in AC are highlighted at different angular positions of the analyser, i.e. at different working positions on the rocking curve [191–196] (see table 6). For example, if the peak of the rocking curve is chosen, only photons experiencing little or no deflection traversing the sample are transmitted by the analyser, ensuring an optimal scatter rejection. Conversely, by setting the orientation of the analyser crystal in one slope of the rocking curve, the system becomes sensitive to refracted photons, which are transmitted with a higher (lower) probability if the refraction angle is towards the top (tail) of the rocking curve [191–193,196]. The overall effect of the analyser orientation on AC radiographs is the edge enhancement of tissue boundaries and of highly oriented structures such as collagen, delineated as bright or dark fringes. Similarly, defects within AC are noticeable, and rendered differently depending on the analyser angle [191,212].

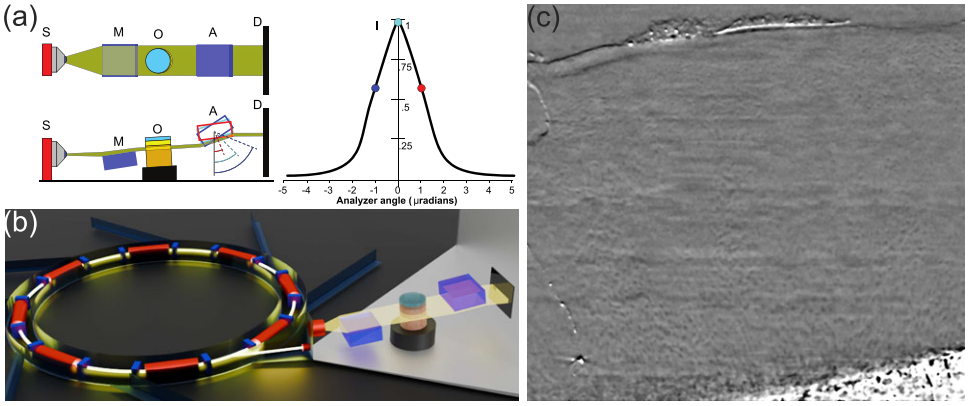

Figure 6. (a) Scheme of ABI. The insertion of the analyser crystal A acts as an angular filter on the photons transmitted by the sample O. Only photons satisfying the angular acceptance, determined by the rocking curve (on the right-hand side), are transmitted by the analyser A and reach the detector D. (b) Three-dimensional rendering of a typical ABI set-up. The ABI requires monochromatic and laminar X-ray beam, typically provided by synchrotron facilities. (c) Section from reconstructed ABI volume of healthy human AC. Margins of AC are highlighted, as well as the speckle pattern conferred by the distribution of chondrocytes' lacunae. Image adapted from the woek of Nagarajan *et al.* [184], published under Creative Commons license (CC BY 4.0).

With the advent of digital detectors, ABI shifted toward tomographic applications, enabling three-dimensional reconstructions of joints from various models, at superior spatial resolutions compared to CT and MRI [198,199,206]. The efficacy of ABI was also assessed on whole intact human knee joints, despite the prolonged exposure time and limited vertical aperture of the X-ray beam [209]. Aside from the clear distinction of macroscopic structures, ABI is also suitable for the imaging of AC microarchitecture. The high sensitivity to subtle changes in the refraction index allows for the depiction of collagen arcades [213] and lacunae [210], down to the spatial resolution of a few μm. High-resolution ABI further enabled cellular characterization of healthy and osteoarthritic AC, distinguishing chondrocyte alignment, zonal distribution and fibrillation [184,197,200,207] (see figure 6c). Different algorithms of phase extraction from ABI images were also studied, and their performance was compared on a common AC sample. Weighting the advantages and pitfalls of the single approaches, those yielding the independent reconstruction of apparent absorption, refraction and scattering signals resulted in the best visualization [204,205].

Interestingly, several studies exploited ABI for its multimodal potential. Rather than the refraction component alone, Muehleman and colleagues applied the method known as multiple-image radiography (MIR) to the visualization of AC. MIR consists in the acquisition of multiple images (i.e. more than three) at several positions of the rocking curve. By using 11 different crystal orientations, the researchers explored the suitability of MIR in detecting a ultrasmall-angle X-ray scattering (USAXS) signal with high precision. Notably, the scattering image distinguished the connective tissues, owing to their inner collagen arrangement [211]. The latter approach was later extended to conventional and limited-angle tomography techniques [201].

Only a few studies implemented ABI with table-top systems. The requisite of monochromaticity is satisfied also by kilovoltage tubes with the adoption of monochromator crystals, although the X-ray beam flux results were significantly reduced [203]. The refraction component clearly depicts AC from other soft tissues in intact joints, and distinguishes AC samples at different degradation stages, with results comparable to histology [202,208]. Nonetheless, the implementation of ABI to table-top systems remains the most challenging compared to other PC techniques.

(iii) Grating interferometry (GI)

Grating interferometry (GI) is based on the Talbot self-image effect produced by regular periodic structures with a period in the order of a few micrometers, referred to as gratings, set along the direction of propagation of the X-rays. Owing to Fresnel diffraction, diffraction patterns with

Table 6. Summary of research papers including X-ray imaging of AC with ABI protocols, ordered from the most to the least recent. For each paper, the corresponding reference is reported, along with the model for the AC tissue, the size of the specimen *S*, the source type, the energy *E* of the X-ray beam (m., monochromatic; q.m., quasi-monochromatic), the number of analyser positions N_A, the acquisition time *T* and the voxel size of the reconstructed volume *p*.

ref.	model	size (mm)	source	*E*	N_A	*T* (min)	*p* (μm)
[188]	rat	NA	synchrotron	20–35 keV m.	NA	NA	9
[197]	human	NA	synchrotron	26 keV q.m.	NA	NA	8
[198]	rabbit	NA	synchrotron	51 keV m.	2	10–60	46
[199]	swine	NA	synchrotron	40 keV m.	5	NA	18.7
[184,200]	human	Ø 7	synchrotron	26 keV q.m.	NA	NA	8
[201]	human	NA	synchrotron	40 keV	25	NA	50
[186]	human	NA	synchrotron	40 keV m.	1	5	31.2
[202]	equine	80x35x30	X-ray tube	22.15 keV m.	17	NA	160; 153
[203]	human	NA	X-ray tube	22.15 keV m.	15	240	160; 153
[204]	human	Ø 7	synchrotron	26 keV m.	5	NA	16
[205]	human	Ø 8	synchrotron	25 keV m.	5	NA	16
[206]	guinea pig	NA	synchrotron	52 keV m.	NA	NA	47
[207]	human	Ø 7	synchrotron	26 keV m.	1	NA	8
[208]	human	NA	X-ray tube	59 keV m.	NA	NA	50
[209]	human	NA	synchrotron	51 keV m.	1	1380	56.2
[210]	human	Ø 2.6	synchrotron	20 keV m.	1	7000	3.6
[185]	murine	NA	synchrotron	15 keV m.	2	NA	NA
[187]	canine	NA	synchrotron	40 keV m.	3	NA	50
[211]	human	NA	synchrotron	40 keV m.	11	NA	NA
[189]	human	NA	synchrotron	NA	5	NA	NA
[212]	human	NA	synchrotron	20–50 keV m.	1–3	NA	NA
[190]	human	NA	synchrotron	30 keV m.	3	0.2	50
[196]	human	20	synchrotron	15 keV m.	NA	NA	50
[213]	human	40x60, Ø 15	synchrotron	17/25 keV m.	NA	NA	5
[195]	human	NA	synchrotron	40 keV m.	2	NA	50
[194]	human	Ø 15	synchrotron	17 keV m.	NA	NA	NA
[193]	rabbit	NA	synchrotron	30 keV m.	3	NA	NA
[192]	human	NA	synchrotron	40 keV m.	5	10; 0.5	50–75
[191]	human	NA	synchrotron	18/30 keV m.	NA	0.07–0.1	50

the same periodicity of the grating are formed at specific distances from the grating, which are equal to multiples of the Talbot distance [183]. The first GI studies exploited the spatially coherent synchrotron X-ray beam and made use of two gratings, referred to as G1 and G2, generally positioned downstream from the sample [214,215]. The grating G1, referred to as the phase-grating, is set close to the sample and it is made ideally of X-ray transparent materials, introducing a periodic phase-shift that is responsible for the Talbot diffraction pattern. The grating G2, referred to as the absorption grating, is positioned at a multiple of the Talbot distance and acts as an analyser, partially absorbing the X-rays. As a function of the relative displacement or

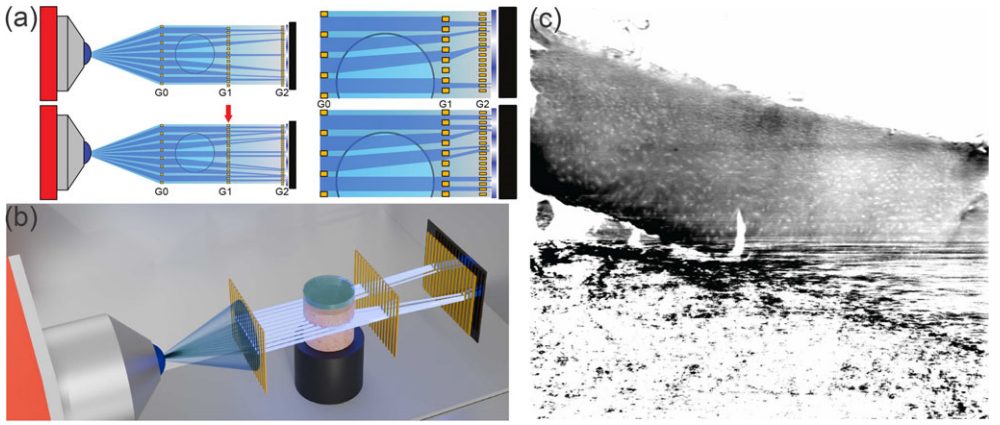

Figure 7. (a) Scheme of GI, in Talbot–Lau configuration. Provided the spatial coherence of the X-ray beam, only the sample gratings G1 and the detector gratings G2 are required. Otherwise, source gratings G0 are required, as in the depicted case. The distance of the detector gratings is determined according to the occurrence of the Talbot self-image effect. The lateral shift of the detector gratings allows to collect the refraction and the scattering signals. (b) Three-dimensional rendering of a typical Talbot–Lau GI set-up, featuring a conventional X-ray source (e.g. X-ray tube). (c) Section from reconstructed GI volume of healthy human AC. Within AC, spots featuring higher intensity are distinguishable, attributable to chondrocytes' lacunae. Image adapted from the work of Schulz *et al.* [218], published under Creative Commons license (CC BY 3.0).

misalignment of the two gratings, a modulation in the X-ray intensity recorded at the imaging plane is observed. Similarly to ABI, when a sample is introduced in the beam, the recorded intensity is modified according to the sample's attenuation, phase and scattering properties, which can be retrieved using a dedicated algorithm [216]. In the wake of these SR-based results, Pfeiffer and colleagues successfully adapted GI to conventional low-brilliance X-ray sources [148]. To overcome the smearing of the diffraction pattern that would occur using a source with limited spatial coherence, a third absorption grating close to the source, is inserted into the so-called Talbot–Lau configuration. The source grating G0 generates a periodic array of repeated sharp line sources which are individually coherent despite being globally non-coherent. This arrangement produces a diffraction pattern which, as in the Talbot case, can be transformed into intensity modulations at the detector plane by displacing G1 and G2 [217]. The Talbot–Lau scheme for GI is displayed in figure 7.

Since its inception, GI has been applied to the visualization of articular soft tissues. SR implementations of GI allowed a good delineation of the edges of AC [219–221]. Similarly, laboratory-based GI set-ups using polychromatic and non-point-like focal spot sources have delivered differential PC images enabling the visualization of AC [222–224] (see table 7). Advances in grating fabrication promoted the translation of GI to clinical settings, with *ex vivo* studies on human metacarpophalangeal joints highlighting AC margins [230,232,233,235], followed by optimized low-dose *in vivo* imaging of healthy volunteers [230–232,235]. More recently, a conventional X-ray tube-driven GI system has been tested for the assessment of rheumatoid arthritis, to ascertain its sensitivity to tissue alterations. Independent evaluations, namely, MRI and clinical scores, have supported the results, suggesting that the GI apparatus distinguishes healthy AC from pathological tissue [226]. Albeit the promising results in terms of AC visibility, the works reported until now have focused on GI to radiography, as the tomographic implementation would raise further concerns on deposited dose.

In the research frame, the translation of GI to tomography delivers three-dimensional maps of absorption, refraction and scattering (or DF) components [228,234]. The refraction-enhanced method highlighted AC microstructures such as chondrocyte clusters, while energy-dependent protocols enabled simultaneous imaging of mineralized and soft tissues [218,229] (see figure 7c).

Table 7. Summary of research papers including X-ray imaging of AC with GI protocols, ordered from the most to the least recent. For each paper, the corresponding reference is reported, along with the model for the AC tissue, the size of the specimen S, the source type (Mo, molybdenum; W, tungsten), the focal spot size s_{FS}, the voltage V or associated energy E of the X-ray beam (m., monochromatic), the number of grating positions N_G, the acquisition time T and the voxel size of the reconstructed volume p.

ref.	model	S (mm)	source	s_{FS} (μm)	V/E	N_G	T (min)	p (μm)
[225]	porcine	Ø 3	synchrotron	NA	20 keV m.	5	20	4.46
[226]	human	NA	X-ray tube (W)	400	40 kVp	NA	0.32	85
[227]	bovine	Ø 6	X-ray tube (Mo)	400	40 kVp	11	NA	41
[228]	human	Ø 5.4	X-ray tube	0.9–2.7	42 kVp	7	NA	23.3
			synchrotron		19 keV	NA	2.3	23.3
			synchrotron		52 keV	NA	5.1	23.3
[218]	human	Ø 5	synchrotron	NA	19 keV	5	NA	2.3
		Ø 5	X-ray tube	NA	40 kVp	5	NA	3
		entire knee	X-ray tube	NA	180 kVp		1020	65
[229]	human	Ø 5	X-ray tube	NA	52 keV	4	NA	5.1
		Ø 10	synchrotron	NA	19 keV	5	NA	2.3
[230]	human	NA	X-ray tube (W)	300	40 kVp	5	0.25	85
[231]	human	NA	X-ray tube (W)	450	40 kVp	3	19	85
[232]	human	NA	X-ray tube (W)	400	40 kVp	3	19	90
[219]	porcine	NA	X-ray tube (W)	300	49 kVp	NA	NA	NA
[220]	porcine	NA	X-ray tube (W)	300	49 kVp	NA	NA	NA
[233]	human	NA	X-ray tube (W)	300	40kVp	5	NA	85
[221]	chicken	NA	synchrotron	NA	17.5 keV m.	NA	0.008	12
					35 keV m.			
[234]	human	Ø 8	synchrotron	NA	32 keV m.	3	NA	16
[235]	human	NA	X-ray tube (W)	60	40 kVp	NA	NA	50
				300	40 kVp	16	NA	50
[222]	chicken	NA	X-ray tube (W)	300	40 kVp	NA	NA	NA
[223]	chicken	NA	X-ray tube (W)	300	40 kVp	NA	NA	NA
[224]	chicken	NA	X-ray tube (W)	300	40 kVp	NA	0.67	18

GI imaging also reportedly revealed differences in collagen content between superficial and deep AC layers. These variations reflect the gradient of electron density related to collagen content, making GI a quantitative tool complementary to state-of-the-art MRI maps. Note that GI imaging is not prone to biases induced by variation in water content, unlike MRI. In this aspect, GI could provide sound information of ECM integrity, regardless of the interstitial fluid [227].

(iv) Edge-illumination imaging

Edge illumination (EI) imaging allows access to phase information by means of regular absorbing structures (i.e. masks) with a period in the order of tens of micrometers, positioned along the X-ray propagation direction [149]. A typical EI set-up features two masks, positioned upstream of the sample (M1) and close to the detector (M2), respectively. Each mask is structured as a linear array of absorbing material, such as gold, interleaved with X-ray transparent septa, or apertures,

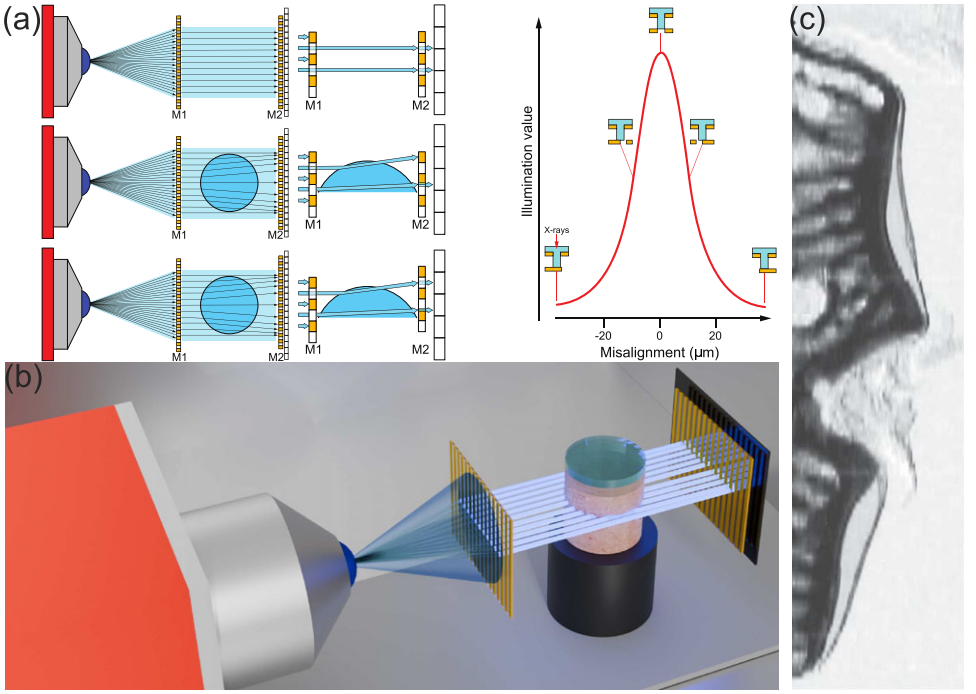

Figure 8. (a) Scheme of EI imaging. When illuminated, the sample mask M1 and the detector mask M2 produce an illumination pattern, replicating the periodicity of the masks. The overall effect of masks' lateral displacements on the intensity modulation of a single pixel is summarized by the illumination curve (on the right-hand side). The insertion of the sample modifies the illumination pattern, according to interactions of different nature. In particular, the absorption, the refraction and the scattering of photons either attenuate, deviate or broaden the beamlets, and alter the modulation of the illumination curve. The lateral shift of the detector mask M2 allows the retrieval of those signals, as different sensitive areas of detector are differentially exposed. (b) Three-dimensional rendering of a typical EI set-up. As reported in literature, nearly all experiments featured conventional X-ray sources (e.g. X-ray tubes). (c) Planar image of 1 mm section from healthy murine osteochondral tissue. Besides the depiction of mineralized tissues (black structures), the interface of AC is clearly recognizable. Image adapted from the work of Marenzana *et al.* [236], published under Creative Commons license (CC BY 3.0).

with a dimension of a few micrometers. Both masks share the same periodicity and aperture size, apart from the geometrical magnification factor, depending on their relative position with respect to the X-ray source. The masks' period matches the detector pixel pitch, such that each periodic feature of the mask corresponds to one detector pixel column (or row). The role of mask M1 is to structure the incoming X-ray beam into a series of independent, non-interfering narrow beams, or beamlets. In the absence of a sample, when the apertures of mask M2 are aligned with the apertures of M1, the beamlets are fully transmitted to the detector. If M1 and M2 are laterally displaced, the transmission decreases (ideally) reaching zero if the apertures are completely misaligned. The resulting curve, describing pixel-by-pixel the X-ray transmission across the two masks as a function of their lateral displacement, is known as the illumination curve and plays a role conceptually analogous to the rocking curve in ABI. When a sample is introduced, the illumination curve is modulated in terms of area, owing to X-ray absorption, lateral position, owing to refraction and width, owing to scattering. A scheme of EI principles of image formation is shown in figure 8. By using suitable retrieval algorithms and acquiring images at (at least) three positions on the illumination curve, all these effects can be uncoupled, producing attenuation, phase and DF maps of the sample [237]. Although GI and EI share some similarities, EI is a non-interferometric technique as the beamlets are sufficiently spaced to be individually analysed, hence not relying on the formation of diffraction patterns. As for the

Table 8. Summary of research papers including X-ray imaging of AC with EI protocols, ordered from the most to the least recent. For each paper, the corresponding reference is reported, along with the model for the AC tissue, the size of the specimen *S*, the source type, the voltage *V* or associated energy *E* of the X-ray beam (m., monochromatic), the number of mask positions N_M, the acquisition time *T* and the voxel size of the reconstructed volume *p*.

ref.	model	*S* (mm)	source	*V*/*E*	N_M	*T* (min)	*p* (μm)
[238]	chicken	NA	X-ray tube	40 kVp	NA	0.03	NA
[236]	murine	NA	X-ray tube	40 kVp	NA	NA	9
		NA	synchrotron	17 keV m.	NA	NA	5
[239]	rat	NA	X-ray tube	NA	NA	NA	NA
[240]	rat	NA	X-ray tube	40 kVp	4	1	20

Talbot–Lau GI, the EI configuration does not require strict constraints on X-ray source coherence and it is implemented with commercial, polychromatic X-ray sources [135,237].

In the context of AC imaging, EI has been mostly implemented within table-top systems (see table 8). Notably, differently from all other mentioned techniques, the spatial resolution of an EI system is not related to the size of the X-ray focal spot or to the detector pixel size, but it is ultimately determined by the aperture size of the pre-sample mask, allowing an additional degree of flexibility in trading-off acquisition time and image quality [149,241,242]. The research group at University College London, who pioneered EI, demonstrated the viability of EI implemented with an uncollimated and non-microfocus X-ray tube, for the visualization of small lesions in rat AC [240]. Despite the relatively thin AC layer, EI images provided visualization in both air and aqueous environments. The measurements of tissue thickness were comparable to CE-based studies and gold standard techniques, such as histology [236,239]. The yield in refraction images are comparable to the synchrotron-based ABI system and confirms the soundness of using the refraction signal to highlight the AC layer [236] (see figure 8c). One further implementation of EI has considered the insertion of a structured detector to replace the detector mask (M2), demonstrating a clear visualization of AC in the refraction image, similarly to conventional EI set-up [238].

(c) Scattering-based X-ray imaging: dark-field (DF) imaging

DF imaging conveys contrast from USAXS photons, which arise from the interaction of primary X-rays with microscopic structures in the sample. These structures are typically not resolved with conventional attenuation-based techniques, owing to insufficient spatial resolution or to the low radiopacity of the structures [217]. Under the ray tracing approximation, USAXS can be understood as the effect of multiple refraction causing locally a diffusion of the X-ray beam. The amount of diffusion can be traced back to quantities such as the average size of the scatterers or the scattering power of the sample, hence giving access to information at a spatial scale below the system's spatial resolution [217,243–245]. As anticipated in the previous subsections, many PC methods including ABI, GI and EI give access to the scattering signal, generally at the cost of additional exposures at different positions of the optical element.

DF imaging has been explored as a complementary signal for assessing soft tissues, including AC, alongside PC refraction-based methods. Since the first studies, results demonstrated the ability of DF in depicting features of AC at a sub-pixel spatial resolution. Early applications included film-based DF radiographies acquired with the ABI technique, which highlighted the soft tissue components of excised human joints in different environmental conditions [243,246–248]. The same approach was also followed on intact joints, where the differentiation of AC structures resulted as optimal, given a careful selection of orientations of the analyser crystal [249,250]. In particular, different orientations conferred major contrast to AC contour or bulk

Table 9. Summary of research papers including X-ray imaging of AC with DF protocols, ordered from the most to the least recent. For each paper, the corresponding reference is reported, along with the model for the AC tissue, the size of the specimen *S*, the source type, the size of the focal spot s_{FS} (Cu copper), the voltage *V* or associated energy *E* of the X-ray beam (m., monochromatic; p.b., pink beam), the acquisition time *T* and the voxel size of the reconstructed volume *p*.

ref.	model	*S* (mm)	source	s_{FS} (μm)	*V*/*E*	*T* (min)	*p* (μm)
[252]	rabbit	1	X-ray tube (Cu)	350	8 keV m.	NA	1.1[a]
[253]	equine	2x0.5x0.5	synchrotron	NA	25 keV p.b.	5	0.8
			X-ray tube (Cu)	350	8 keV m.	NA	1.1[a]
[246]	human	NA	synchrotron	NA	20 keV m.	NA	7.4
					12 keV m.	NA	16
[243]	human	NA	synchrotron	NA	35 keV m.	NA	10
[254]	human	NA	synchrotron	NA	36 keV m.	0.92	NA
[251]	human	NA	synchrotron	NA	36 keV m.	NA	NA
[249]	human	NA	synchrotron	NA	34.8 keV m.	NA	NA
					33 keV m.	NA	NA
[250]	human	NA	synchrotron	NA	34.8 keV m.	NA	NA
[247]	human	NA	synchrotron	NA	35 keV m.	NA	10
[248]	human	NA	synchrotron	NA	15 keV m.	NA	NA

[a]Detector pitch size.

[251]. Notwithstanding the promising results in radiography, the rather large number of frames required at different orientations of the analyser significantly increases the radiation dose and the exposure time, thus limiting the translation of ABI-based DF imaging to SR-based CT (see table 9). On the other hand, the tomosynthesis approach requires fewer projection images, compared to CT, while giving a certain level of in-depth information. Notably, past works delivered DF tomosyntheses with doses equivalent to a single DF radiograph [254]. Recently, the feasibility of DF has been demonstrated on alternative experimental designs. Specifically, thanks to the beam-tracking technique, which is an EI variant making use of a high-resolution detector instead of the M2 mask [255], DF, refraction and attenuation images of AC could be obtained simultaneously [227]. From these images, authors speculated the visualization of collagen bundles. Further radiographs performed with the same imaging configuration properly visualized lacunae of AC [252]. Despite the two-dimensional nature, the cellular pattern was compatible to reference images from synchrotron-driven PBPC method and histology [253].

3. Towards the *in situ* evaluation of articular cartilage

Originally conceived for trabecular bone characterization [256], DVC has been applied to various musculoskeletal tissues [257–260]. Its principles include the tracking of recognizable voxel-intensity variations through sequential compression steps, the evaluation of displacement vectors, and the derivation of the strain tensor field [261]. In the case of AC, time-resolved rheologic experiments require multiple rapid tomographic scans, yielding speckled patterns obtained under different compressive steps. To the aims of DVC, the lacunae hosting chondrocytes serve as discrete patterns ideal for strain measurements. Such patterns can be highlighted with several approaches. In absorption mode, CAs such as the polyoxometalates enhance the contrast between the lacunae and the surrounding ECM [40], though fixation and staining alter the mechanical properties of the tissue. Alternatively, novel staining protocols could lead to the preservation of the original mechanical behaviour of AC [15,24]. Furthermore, DNA-binding stains enhance

lacunae visibility [39], but require complex processing procedures and a severe downsizing of the sample. The combination of PC with CAs was also investigated to highlight features of AC and compensate the limited flux and coherence of laboratory microCT systems [9,171–177] (see table 5). However, the limited X-ray flux implies prolonged scan times, with significant effect on AC properties and sample stability [156]. SR microCT overcomes these issues thanks to the availability of high flux X-ray beams.

For instance, a methodology to visualize and quantify cellular structures in compressed AC was recently proposed, along with a dedicated SR beamline [157]. In the same beamline, the compressive method with DVC was also implemented on a murine model, and yielded the visualization of hierarchical changes in AC structures. The high spatial resolution reached (0.8 µm), allowed the calculation of displacements with accuracies below 100 nm in knees of healthy and osteoarthritic mice [158].

In addition to PBPC, the investigation of osteochondral samples under compression was accomplished with other PC methods. At the SPring-8 synchrotron facility in Japan, GI-microCT successfully resolved the cellular pattern of porcine AC, as confirmed by histology. The deformation of the cellular pattern served as input for DVC analysis. Remarkably, the density map of sample was shown to change accordingly to the imparted compression [225].

Despite the positive outcome of the above-described implementations, most studies making use of PC techniques require a scanning or stepping of optical elements. As a result, they are focused on imaging of AC in a static configuration, because of the longer times related to acquisition procedures and the limited time-resolving capabilities of laboratory-based systems, associated to the limited X-ray flux. Interestingly, the time-resolved approach was successfully implemented with PBPC, exploiting monochromatic SR. Its implementation was demonstrated at TOMCAT beamline, at the Paul Scherrer Institute in Switzerland, where a rheometric set-up allowed the evaluation of dynamic behaviour through time of unprocessed bovine AC samples [152]. The tomographic experiment took advantage of the shortest exposure time to date for the dynamic investigation of connective tissues, resulting in acquisition times ranging from 40 down to 5 seconds. The advantageous experimental condition achieved spatial resolutions compatible with the size of lacunae (2.75 µm), with nearly no radiation damage caused to the tissue. Notwithstanding the detrimental laminarization of the monochromatized beam, the experiment benefited from a field of view large enough to accommodate the whole AC (5.54 × 3.85 mm against 4 mm diameter samples). According to existing literature, PBPC is the most straight-forward implementation for rheometric measurements. It offers favourable acquisition time and image quality, while keeping as low as possible the complexity of the experimental set-up.

4. Benefits, challanges and future perspectives

The above discussed X-ray imaging techniques achieve optimal results in terms of contrast and detail discernability of AC, in a variety of models and experimental conditions. Nevertheless, the choice of the imaging approach should be tailored to the rationale of the investigation. The relatively large number of studies applying CAs reflects the straightforward implementation of CECT to AC imaging. The use of ionic CAs allows for a quantitative analysis of several components of AC (see table 1). Nevertheless, their possible effect on the tissue's mechanical properties draws concerns in rheologic applications. For instance, hyperosmolar CA solutions modify tissue stiffness [262–264]. Furthermore, certain staining protocols alter the mechanical response of the tissue and introduce significant bias in rheometric evaluation of the whole osteochondral unit [15].

In addition, the composition of CAs should be chosen to optimize the imaging outcome. The imaging protocol should include X-ray energies compatible with the absorption signature of the selected radiopaque element. In the context of spectral protocols, this aspect becomes more crucial. In fact, mixtures of CAs with different absorbing features facilitate the material discrimination [265]. Furthermore, the CA concentration should be carefully chosen to

simultaneously yield the optimal contrast among details and reduce imaging artifacts. Despite its readiness, the use of CAs with conventional microCT scanners could impair the segmentation of tissues with similar radiopacity, as in the case of contrast-enhanced AC and mineralized tissues [105].

Spectral approaches such as the DE technique could circumvent the issue, yet it still faces several limitations. First, multiple acquisitions require volume co-registration in space or in time, whether images are collected with two sources at different spatial locations simultaneously, or with a single source at different time points, respectively. Second, the span of materials is restricted by the limited flexibility of spectra provided by conventional X-ray sources. Third, the material decomposition worsens if the number of materials entering the composition of the sample exceeds the beam energies [265]. Last, radiation dose increases with the number of energy exposures. PCDs overcome these limitations, although their larger pixel sizes and/or smaller field-of-view limit the spatial resolution. The development of the latest PCD technologies (i.e. modular structure and advanced signal clustering) allows a larger field of view, and a resolution finer than the pixel pitch [266,267].

PC techniques enable the visualization of several structures in AC (namely, collagen arcades, lacunae and even chondrocytes) [2,152,154,164,197,207,218,225,229] without exogenous CAs, though most approaches require high-brilliance sources, *ad hoc* optics, or their combination. Propagation-based PC is the most promising method for rheologic evaluation of AC, provided the implementation with SR [152]. The same considerations apply to ABI, plus the additional limitations related to the use of monochromatic X-ray beams, laminar geometry and the need for multiple scans at different analyser orientations. Similarly to ABI, GI is a multimodal approach sensitive to refraction and scattering signals, delivering promising results *in vivo* [226]. In research-oriented applications, GI allows for the visualization of cellular patterns in AC, pushing its applications to *in situ* testing of AC [225]. Nonetheless, high-end applications of GI make the implementation with SR essential, to compensate for the prolonged acquisition times associated with multiple-frame grating stepping. The rigorous requirements on X-ray beam decay for non-interferometric EI, as it is easily implemented to compact laboratory-based systems. Furthermore, EI potentially retrieves phase information with only two images, by illuminating the pixels at their opposite sides, compared to the GI method [268]. Nevertheless, studies adopting EI for AC imaging are in the minority, with no reported experience on *in situ* evaluations. Focusing on the scattering signal, DF imaging is still under development, specifically for AC evaluation. Despite the unique nature of the signal, DF imaging has been mainly limited to plain radiographs or tomosynthesis only, as the tomographic approach would significantly increase the acquisition times and the dose fractions.

Aside from in-depth analysis of the single techniques, more general observations arise by considering the examined literature. In general, high resolution is obtained at the cost of reduced sample size, increased photon fluxes and greater radiation doses. Furthermore, the evaluation of mechanical response requires volumes representative of the whole tissue (i.e. ECM), rather than single structures (i.e. collagen bundles). Recently, an imaging protocol has been proposed as optimal trade-off between the sample size and spatial resolution for the visualization of lacunae, in the context of time-resolved *in situ* imaging [152].

Another concern arises from the time of exposure to radiation. The scanning time of each technique is largely dependent on the X-ray source characteristics, the presence of optical elements and the geometrical configuration. SR generally ensures the fastest exposure times, especially when the full spectrum (i.e. white beam) is used coupled to the PBPC technique. Conversely, the installation of any optical element in the beam generally leads to longer exposure times both at synchrotrons and laboratory-based systems.

Radiation dose remains a major concern. Planar and tomosynthesis studies report mGy-level exposures compatible with clinical translation [163,209,231,233,246], while tomographic experiments may reach several Gy, inducing macroscopic (namely, heating of the sample) [40,269] and microscopic (namely, degradation of ECM, oxidative stress and cellular degeneration) effects [9,117,118,152,163,209] (see table S4 in the electronic supplementary material). Furthemore, the

evaluation of the whole osteochondral unit should consider significant effects of prolonged X-ray exposures on bone tissues [270,271]. Therefore, any rheologic experiment should consider cryogenic expedients compensating the progressive dose deposition, with special mention to SR studies.

Aside from rheologic applications, more relaxed experimental conditions for AC imaging meet the use of multimodal laboratory-based X-ray systems. Preliminary experiences retrieved successfully attenuation, differential PC and DF channels on biological samples [135]. Similar to the multimodal X-ray system involved in the work of Olivo *et al.*, the equipment installed at PEPILab features specifications meeting the depiction of AC structures. In the perspective of preclinical applications, a CT prototype has been developed to deliver USAXS images. Its application to lung evaluation on healthy humans and patients with pulmonary disorders yielded results comparable to conventional radiography [272,273]. Analogously, applications of DF could be extended to musculoskeletal imaging. For instance, articular soft tissues might be distinguished, as well as their alteration, thanks to the sub-pixel spatial resolution inferred by grating configurations.

5. Conclusion

The present scoping review focused on X-ray techniques adopted for AC imaging. One of the main differentiations accounts for the prompt implementation of these approaches with either commercial systems or synchrotron-driven set-ups. In the first case, CE techniques can be easily implemented with radiopaque CAs. Nonetheless, the use of CAs might alter the pristine properties of the tissue. Conversely, PC methods do not imply any alteration of the AC nature, but require stringent specifications for the X-ray source. The sought-after coherence of the X-ray beam, crucial for PC imaging, is achieved with SR. Thanks to the latter implementation, various optical configurations retrieve valuable information of AC, down to the cellular scale. Regardless of the intrinsic contrast enhancement associated with PC, the limited access to SR facilities hinders the full unfolding of refraction-based imaging modalities. A promising option makes use of conventional X-ray sources, together with suitable optical elements. Still, the low brilliance of conventional sources significantly increases the acquisition times. Finally, the scattering information associated with DF is still under investigation for various biomedical applications, including the musculoskeletal system.

The context becomes further complicated when rheologic studies are considered. Among the approaches here discussed, PC methods provide visual and quantitative information. According to the existing literature, PBPC and GI successfully depict the inner structures of AC and enable their implementation to DVC analysis. Specifically, PBPC features the shortest acquisition time to resolve the microscopic lacunae. In contrast, GI and, in general, PC methods based on optical elements lead to increased exposure times, raising concerns on the deposited radiation dose and sample stability. At present, this limits rheologic evaluation of AC samples mostly to synchrotron-based experiments. However, the development of novel synchrotron-like X-ray sources with a smaller footprint and cost, such as laser-driven system of liquid-metal jet sources, hold the promise to affect AC imaging, enabling advanced applications, such as rheology, in the compact laboratory environment.

Data accessibility. The data are provided in the electronic supplementary material [274].

Declaration of AI use. We have not used AI-assisted technologies in creating this article.

Authors' contributions. S.F.: conceptualization, data curation, formal analysis, investigation, methodology, project administration, software, supervision, validation, visualization, writing—original draft, writing—review and editing; L.B.: conceptualization, data curation, formal analysis, supervision, validation, visualization, writing—review and editing; P.C.: conceptualization, data curation, formal analysis, supervision, validation, visualization, writing—review and editing; F.B.: conceptualization, funding acquisition, investigation, methodology, project administration, resources, supervision, validation, visualization, writing—review and editing.

All authors gave final approval for publication and agreed to be held accountable for the work performed therein.

Conflict of interest declaration. We declare we have no competing interests.

Funding. This research was co-funded by the Italian Complementary National Plan PNC-I.1 'Research initiatives for innovative technologies and pathways in the health and welfare sector' D.D. 931 of 06/06/2022, 'DARE - DigitAl lifelong pRevEntion' initiative, code PNC0000002, CUP: B53C22006230001.

Acknowledgements. We would like to thank Luigi Lena for providing the figures in this paper.

References

1. Mizutani R, Suzuki Y. 2012 X-ray microtomography in biology. *Micron* **43**, 104–115. (doi:10.1016/j.micron.2011.10.002)
2. Zehbe R, Haibel A, Riesemeier H, Gross U, Kirkpatrick CJ, Schubert H, Brochhausen C. 2010 Going beyond histology. Synchrotron micro-computed tomography as a methodology for biological tissue characterization: from tissue morphology to individual cells. *J. R. Soc. Interface* **7**, 49–59. (doi:10.1098/rsif.2008.0539)
3. Mow VC, Ratcliffe A, Poole AR. 1992 Cartilage and diarthrodial joints as paradigms for hierarchical materials and structures. *Biomaterials* **13**, 67–97. (doi:10.1016/0142-9612(92)90001-5)
4. Ateshian GA. 2009 The role of interstitial fluid pressurization in articular cartilage lubrication. *J. Biomech.* **42**, 1163–1176. (doi:10.1016/j.jbiomech.2009.04.040)
5. Setton LA, Elliott DM, Mow VC. 1999 Altered mechanics of cartilage with osteoarthritis: human osteoarthritis and an experimental model of joint degeneration. *Osteoarthr. Cartil.* **7**, 2–14. (doi:10.1053/joca.1998.0170)
6. Mahjoub M, Berenbaum F, Houard X. 2012 Why subchondral bone in osteoarthritis? The importance of the cartilage bone interface in osteoarthritis. *Osteoporos. Int.* **23**, 841–846. (doi:10.1007/s00198-012-2161-0)
7. Dall'Ara E, Pe na-Fernández M, Palanca M, Giorgi M, Cristofolini L, Tozzi G. 2017 Precision of digital volume correlation approaches for strain analysis in bone imaged with micro-computed tomography at different dimensional levels. *Front. Mater.* **4**, 31. (doi:10.3389/fmats.2017.00031)
8. Mourad C, Gallego Manzano L, Viry A, Booij R, Oei EHG, Becce F, Omoumi P. 2024 Chances and challenges of photon-counting CT in musculoskeletal imaging. *Skeletal Radiol.* **53**, 1889–1902. (doi:10.1007/s00256-024-04622-6)
9. Clark J, Garbout A, Ferreira S, Javaheri B, Pitsillides A, Rankin S, Jeffers J, Hansen U. 2020 Propagation phase-contrast micro-computed tomography allows laboratory-based three-dimensional imaging of articular cartilage down to the cellular level. *Osteoarthr. Cartil.* **28**, 102–111. (doi:10.1016/j.joca.2019.10.007)
10. Lusic H, Grinstaff MW. 2013 X-ray-computed tomography contrast agents. *Chem. Rev.* **113**, 1641–1666. (doi:10.1021/cr200358s)
11. Pauwels E, Van Loo D, Cornillie P, Brabant L, Van Hoorebeke L. 2013 An exploratory study of contrast agents for soft tissue visualization by means of high resolution X-ray computed tomography imaging: contrast agents for soft tissue visualization with microct. *J. Microsc.* **250**, 21–31. (doi:10.1111/jmi.12013)
12. Omelchenko AI, Dyachkova IG, Zolotov DA, Kaloyan AA, Shepeleva VO, Podurets KM. 2024 New approaches in the tomographic visualization of joints using X-ray contrast nanoparticles and laser radiation. *Crystallogr. Rep.* **69**, 214–219. (doi:10.1134/S1063774524600011X)
13. Nelson BB *et al.* 2024 Longitudinal in vivo cationic contrastenhanced computed tomography classifies equine articular cartilage injury and repair. *J. Orthop. Res.* **42**, 2264–2276. (doi:10.1002/jor.25869)
14. Jäntti J *et al.* 2024 Cationic tantalum oxide nanoparticle contrast agent for micro computed tomography reveals articular cartilage proteoglycan distribution and collagen architecture alterations. *Osteoarthr. Cartil.* **32**, 299–309. (doi:10.1016/j.joca.2023.11.020)
15. Davis S, Karali A, Balcaen T, Zekonyte J, Pétré M, Roldo M, Kerckhofs G, Blunn G. 2024 Comparison of two contrast-enhancing staining agents for use in X-ray imaging and digital volume correlation measurements across the cartilage-bone interface. *J. Mech. Behav. Biomed. Mater.* **152**, 106414. (doi:10.1016/j.jmbbm.2024.106414)

16. Valerio MS, Edwards JB, Dolan CP, Motherwell JM, Potter BK, Dearth CL, Goldman SM. 2023 Effect of targeted cytokine inhibition on progression of post-traumatic osteoarthritis following intra-articular fracture. *Int. J. Mol. Sci.* **24**, 13606. (doi:10.3390/ijms241713606)
17. Borges N, Das P, Forte A, Vincent T, Dini D, Marenzana M. 2014 Rapid, automated imaging of mouse articular cartilage by microCT for early detection of osteoarthritis and finite element modelling of joint mechanics. *Osteoarthr. Cartil.* **22**, 1419–1428. (doi:10.1016/j.joca.2014.07.014)
18. Lin A, Reece D, Thote T, Sridaran S, Stevens H, Willett N, Guldberg R. 2023 Intra-articular delivery of micronized dehydrated human amnion/chorion membrane reduces degenerative changes after onset of post-traumatic osteoarthritis. *Front. Bioeng. Biotechnol.* **11**, 1224141. (doi:10.3389/fbioe.2023.1224141)
19. Jo S, Sebro R. 2023 *In vivo* intra-articular contrast enhanced μCT imaging of mouse knee cartilage. *Bone* **167**, 116632. (doi:10.1016/j.bone.2022.116632)
20. Jin Y, Park D, Noh S, Kwon H, Shin D, Park J, Min BH. 2023 Effects of glycosaminoglycan content in extracellular matrix of donor cartilage on the functional properties of osteochondral allografts evaluated by micro-CT non-destructive analysis. *PLoS ONE* **18**, e0285733. (doi:10.1371/journal.pone.0285733)
21. Honkanen M *et al.* 2023 Dual-contrast micro-CT enables cartilage lesion detection and tissue condition evaluation ex vivo. *Equine Vet. J.* **55**, 315–324. (doi:10.1111/evj.13573)
22. Fleischer M, Hartner S, Newton M, Baker K, Maerz T. 2023 Early patellofemoral cartilage and bone pathology in a rat model of noninvasive anterior cruciate ligament rupture. *Connect. Tissue Res.* **64**, 175–185. (doi:10.1080/03008207.2022.2136571)
23. Durongbhan P, Silva M, Li Z, Ansari N, Kour R, Davey C, Stok K. 2023 A microCT imaging protocol for reproducible and efficient quantitative morphometric analysis (QMA) of joint structures of the in situ mouse tibio-femoral joint. *Bone* **166**, 116606. (doi:10.1016/j.bone.2022.116606)
24. Davis S, Karali A, Zekonyte J, Roldo M, Blunn G. 2023 Development of a method to investigate strain distribution across the cartilage-bone interface in guinea pig model of spontaneous osteoarthritis using lab-based contrast enhanced X-ray-computed tomography and digital volume correlation. *J. Mech. Behav. Biomed. Mater.* **144**, 1–7. (doi:10.1016/j.jmbbm.2023.105999)
25. Chan D, Mashiatulla M, Li J, Ross R, Pendyala M, Patwa A, Grinstaff M, Plaas A, Sumner D. 2023 Contrast-enhanced micro-computed tomography of compartment and time-dependent changes in femoral cartilage and subchondral plate in a murine model of osteoarthritis. *Anat. Rec.* **306**, 92–109. (doi:10.1002/ar.25027)
26. Bhattarai A, Lok JT, Sun H, Vardhanabhuti V. 2023 Computed tomography of cartilage: an exploration of novel cationic bismuth contrast agent. *Ann. Biomed. Eng.* **51**, 977–986. (doi:10.1007/s10439-022-03110-z)
27. McKinney J *et al.* 2022 Sodium alginate microencapsulation of human mesenchymal stromal cells modulates paracrine signaling response and enhances efficacy for treatment of established osteoarthritis. *Acta Biomater.* **141**, 315–332. (doi:10.1016/j.actbio.2021.12.034)
28. Fowkes MM, Borges N, Das P, Cacho-Nerin F, Brennan PE, Vincent TL, Lim NH. 2022 Imaging articular cartilage in osteoarthritis using targeted peptide radiocontrast agents. *PLoS ONE* **17**, e0268223. (doi:10.1371/journal.pone.0268223)
29. Fantoni S *et al.* 2022 A cationic contrast agent in X-ray imaging of articular cartilage: pre-clinical evaluation of diffusion and attenuation properties. *Diagnostics* **12**, 2111. (doi:10.3390/diagnostics12092111)
30. Zhu Y, Ponjevic D, Matyas J, Boyd S. 2021 Contrast-enhanced X-ray microscopy of articular cartilage. *Connect. Tissue Res.* **62**, 542–553. (doi:10.1080/03008207.2020.1813121)
31. Ve Koon K *et al.* 2021 Comparison of high-resolution magnetic resonance imaging and micro-computed tomography arthrography for *in-vivo* assessment of cartilage in non-human primate models. *Quant. Imaging Med. Surg.* **11**, 3431–3447. (doi:10.21037/qims-20-116)
32. Nelson B, Stewart R, Kawcak C, Freedman J, Patwa A, Snyder B, Goodrich L, Grinstaff M. 2021 Quantitative evaluation of equine articular cartilage using cationic contrast-enhanced computed tomography. *Cartilage* **12**, 211–221. (doi:10.1177/1947603518812562)
33. Nelson B, Mäkelä J, Lawson T, Patwa A, Snyder B, McIlwraith C, Grinstaff M, Goodrich L, Kawcak C. 2021 Cationic contrast-enhanced computed tomography distinguishes between reparative, degenerative, and healthy equine articular cartilage. *J. Orthop. Res.* **39**, 1647–1657. (doi:10.1002/jor.24894)

34. Lawson T, Joenathan A, Patwa A, Snyder BD, Grinstaff MW. 2021 Tantalum oxide nanoparticles for the quantitative contrast-enhanced computed tomography of *ex vivo* human cartilage: assessment of biochemical composition and biomechanics. *ACS Nano* **15**, 19 175–19 184. (doi:10.1021/acsnano.1c03375)
35. Gao X *et al.* 2021 Influence of fixation on CA4+ contrast enhanced microCT of articular cartilage and subsequent feasibility for histological evaluation. *Am. J. Transl. Res.* **13**, 8921–8937.
36. Flynn C, Hurtig M, Linden A. 2021 Anionic contrast–enhanced microCT imaging correlates with biochemical and histological evaluations of osteoarthritic articular cartilage. *Cartilage* **13**, 1388S–1397S. (doi:10.1177/1947603520924748)
37. Dunham C, Steenbock H, Brinckmann J, Reiter A, Castile R, Chamberlain A, Lake S. 2021 Increased volume and collagen crosslinks drive soft tissue contribution to post-traumatic elbow contracture in an animal model. *J. Orthop. Res.* **39**, 1800–1810. (doi:10.1002/jor.24781)
38. Dufour A *et al.* 2021 Repair of full-thickness articular cartilage defects using IEIK13 self-assembling peptide hydrogel in a non-human primate model. *Sci. Rep.* **11**, 4560. (doi:10.1038/s41598-021-83208-x)
39. Danalache M, Beutler K, Rolauffs B, Wolfgart J, Bonnaire F, Fischer S, Greving I, Hofmann U. 2021 Exploration of changes in spatial chondrocyte organisation in human osteoarthritic cartilage by means of 3D imaging. *Sci. Rep.* **11**, 9783. (doi:10.1038/s41598-021-89582-w)
40. Clark JN, Tavana S, Clark B, Briggs T, Jeffers JR, Hansen U. 2021 High resolution three-dimensional strain measurements in human articular cartilage. *J. Mech. Behav. Biomed. Mater.* **124**, 104806. (doi:10.1016/j.jmbbm.2021.104806)
41. Boos MA, Grinstaff MW, Lamandé SR, Stok KS. 2021 Contrast-enhanced micro–computed tomography for 3D visualization and quantification of glycosaminoglycans in different cartilage types. *Cartilage* **13**, 486S–494S. (doi:10.1177/19476035211053820)
42. Blom R, Mol D, van Ruijven L, Kerkhoffs G, Smit T. 2021 A single axial impact load causes articular damage that is not visible with micro-computed tomography: an *ex vivo* study on caprine tibiotalar joints. *Cartilage* **13**, 1490S–1500S. (doi:10.1177/1947603519876353)
43. Besler B *et al.* 2021 Quantitative measures of bone shape, cartilage morphometry and joint alignment are associated with disease in an ACLT and MMx rat model of osteoarthritis. *Bone* **146**, 115903. (doi:10.1016/j.bone.2021.115903)
44. ter Voert C, Kour R, van Teeffelen B, Ansari N, Stok K. 2020 Contrast-enhanced micro-computed tomography of articular cartilage morphology with ioversol and iomeprol. *J. Anat.* **237**, 1062–1071. (doi:10.1111/joa.13271)
45. Sugasawa T *et al.* 2020 Characterization of osteoarthritis in a medial meniscectomy-induced animal model using contrast-enhanced X-ray microtomography. *Biomedicines* **8**, 56. (doi:10.3390/biomedicines8030056)
46. Reece D, Burnsed O, Parchinski K, Marr E, White R, Salazar-Noratto G, Lin A, Willett N, Guldberg R. 2020 Reduced size profile of amniotic membrane particles decreases osteoarthritis therapeutic efficacy. *Tissue Eng. Part A* **26**, 28–37. (doi:10.1089/ten.tea.2019.0074)
47. Meng H, Quan Q, Yuan X, Zheng Y, Peng J, Guo Q, Wang A, Lu S. 2020 Diffusion of neutral solutes within human osteoarthritic cartilage: effect of loading patterns. *J. Orthop. Transl.* **22**, 58–66. (doi:10.1016/j.jot.2019.10.013)
48. Freedman JD, Ellis DJ, Lusic H, Varma G, Grant AK, Lakin BA, Snyder BD, Grinstaff MW. 2020 dGEMRIC and CECT comparison of cationic and anionic contrast agents in cadaveric human metacarpal cartilage. *J. Orthop. Res.* **38**, 719–725. (doi:10.1002/jor.24511)
49. Cubria M *et al.* 2020 Evaluation of musculoskeletal phenotype of the G608G progeria mouse model with lonafarnib, pravastatin, and zoledronic acid as treatment groups. *Proc. Natl Acad. Sci. USA* **117**, 12 029–12 040. (doi:10.1073/pnas.1906713117)
50. Zhang H, Belev G, Stewart RC, Grinstaff MW, Snyder BD, Wilson DR. 2019 Protocol development for synchrotron contrast-enhanced CT of human hip cartilage. *Med. Eng. Phys.* **73**, 1–8. (doi:10.1016/j.medengphy.2019.08.003)
51. Ylitalo T *et al.* 2019 Quantifying complex micro-topography of degenerated articular cartilage surface by contrast-enhanced micro-computed tomography and parametric analyses. *J. Orthop. Res.* **37**, 855–866. (doi:10.1002/jor.24245)
52. Tsai LC, Cooper E, Hetzendorfer K, Warren G, Chang YH, Willett N. 2019 Effects of treadmill running and limb immobilization on knee cartilage degeneration and locomotor

joint kinematics in rats following knee meniscal transection. *Osteoarthr. Cartil.* **27**, 1851–1859. (doi:10.1016/j.joca.2019.08.001)
53. Steppacher S, Hanke M, Zurmühle C, Haefeli P, Klenke F, Tannast M. 2019 Ultrasonic cartilage thickness measurement is accurate, reproducible, and reliable—validation study using contrast-enhanced micro-CT. *J. Orthop. Surg. Res.* **14**, 67. (doi:10.1186/s13018-019-1099-8)
54. Nelson B *et al.* 2019 Evaluation of equine articular cartilage degeneration after mechanical impact injury using cationic contrast-enhanced computed tomography. *Osteoarthr. Cartil.* **27**, 1219–1228. (doi:10.1016/j.joca.2019.04.015)
55. Michalak GJ, Walker R, Boyd SK. 2019 Concurrent assessment of cartilage morphology and bone microarchitecture in the human knee using contrast-enhanced HR-pQCT imaging. *J. Clin. Densitom.* **22**, 74–85. (doi:10.1016/j.jocd.2018.07.002)
56. McKinney J, Doan T, Wang L, Deppen J, Reece D, Pucha K, Ginn S, Levit R, Willett N. 2019 Therapeutic efficacy of intra-articular delivery of encapsulated human mesenchymal stem cells on early stage osteoarthritis. *Eur. Cells Mater.* **37**, 42–59. (doi:10.22203/eCM.v037a04)
57. Kwok A *et al.* 2019 Knee and hip joint cartilage damage from combined spaceflight hazards of low-dose radiation less than 1 Gy and prolonged hindlimb unloading. *Radiat. Res.* **191**, 497–506. (doi:10.1667/RR15216.1)
58. Gatenholm B, Lindahl C, Brittberg M, Stadelmann V. 2019 Spatially matching morphometric assessment of cartilage and subchondral bone in osteoarthritic human knee joint with micro-computed tomography. *Bone* **120**, 393–402. (doi:10.1016/j.bone.2018.12.003)
59. Dourthe B, Nickmanesh R, Wilson D, D'Agostino P, Patwa A, Grinstaff M, Snyder B, Vereecke E. 2019 Assessment of healthy trapeziometacarpal cartilage properties using indentation testing and contrast-enhanced computed tomography. *Clin. Biomech.* **61**, 181–189. (doi:10.1016/j.clinbiomech.2018.12.015)
60. Reece D, Thote T, Lin A, Willett N, Guldberg R. 2018 Contrast enhanced μCT imaging of early articular changes in a pre-clinical model of osteoarthritis. *Osteoarthr. Cartil.* **26**, 118–127. (doi:10.1016/j.joca.2017.10.017)
61. Nickmanesh R, Stewart RC, Snyder BD, Grinstaff MW, Masri BA, Wilson DR. 2018 Contrastenhanced computed tomography (CECT) attenuation is associated with stiffness of intact knee cartilage. *J. Orthop. Res.* **36**, 2641–2647. (doi:10.1002/jor.24022)
62. Mirahmadi F *et al.* 2018 Aging does not change the compressive stiffness of mandibular condylar cartilage in horses. *Osteoarthr. Cartil.* **26**, 1744–1752. (doi:10.1016/j.joca.2018.08.007)
63. Stewart RC, Patwa AN, Lusic H, Freedman JD, Wathier M, Snyder BD, Guermazi A, Grinstaff MW. 2017 synthesis and preclinical characterization of a cationic iodinated imaging contrast agent (CA4+) and its use for quantitative computed tomography of *ex vivo* human hip cartilage. *J. Med. Chem.* **60**, 5543–5555. (doi:10.1021/acs.jmedchem.7b00234)
64. Saukko A, Honkanen J, Xu W, Väänänen S, Jurvelin J, Lehto VP, Töyräs J. 2017 Dual contrast CT method enables diagnostics of cartilage injuries and degeneration using a single CT image. *Ann. Biomed. Eng.* **45**, 2857–2866. (doi:10.1007/s10439-017-1916-3)
65. Raines A, Shih MS, Chua L, Su CW, Tseng S, O'Connell J. 2017 Efficacy of particulate amniotic membrane and umbilical cord tissues in attenuating cartilage destruction in an osteoarthritis model. *Tissue Eng. Part A* **23**, 12–19. (doi:10.1089/ten.TEA.2016.0088)
66. Nieminen H, Gahunia H, Pritzker K, Ylitalo T, Rieppo L, Karhula S, Lehenkari P, Hæggström E, Saarakkala S. 2017 3D histopathological grading of osteochondral tissue using contrast-enhanced micro-computed tomography. *Osteoarthr. Cartil.* **25**, 1680–1689. (doi:10.1016/j.joca.2017.05.021)
67. Mashiatulla M, Moran M, Chan D, Li J, Freedman J, Snyder B, Grinstaff M, Plaas A, Sumner D. 2017 Murine articular cartilage morphology and compositional quantification with high resolution cationic contrast-enhanced μCT. *J. Orthop. Res.* **35**, 2740–2748. (doi:10.1002/jor.23595)
68. Kün-Darbois JD, Manero F, Rony L, Chappard D. 2017 Contrast enhancement with uranyl acetate allows quantitative analysis of the articular cartilage by microCT: application to mandibular condyles in the BTX rat model of disuse. *Micron* **97**, 35–40. (doi:10.1016/j.micron.2017.03.008)
69. Karhula S, Finnilä M, Lammi M, Ylärinne J, Kauppinen S, Rieppo L, Pritzker K, Nieminen H, Saarakkala S. 2017 Effects of articular cartilage constituents on phosphotungstic acid enhanced micro-computed tomography. *PLoS ONE* **12**, e0171075. (doi:10.1371/journal.pone.0171075)

70. Karhula SS *et al.* 2017 Micro-scale distribution of CA4+ in *ex vivo* human articular cartilage detected with contrast-enhanced micro-computed tomography imaging. *Front. Phys.* **5**, 38. (doi:10.3389/fphy.2017.00038)
71. de Visser H, Weinans H, Coeleveld K, van Rijen M, Lafeber F, Mastbergen S. 2017 Groove model of tibia-femoral osteoarthritis in the rat. *J. Orthop. Res.* **35**, 496–505. (doi:10.1002/jor.23299)
72. Willett N, Thote T, Hart M, Moran S, Guldberg R, Kamath R. 2016 Quantitative preclinical screening of therapeutics for joint diseases using contrast enhanced micro-computed tomography. *Osteoarthr. Cartil.* **24**, 1604–1612. (doi:10.1016/j.joca.2016.04.021)
73. van Tiel J *et al.* 2016 Quantitative *in vivo* CT arthrography of the human osteoarthritic knee to estimate cartilage sulphated glycosaminoglycan content: correlation with *ex-vivo* reference standards. *Osteoarthr. Cartil.* **24**, 1012–1020. (doi:10.1016/j.joca.2016.01.137)
74. Stok K *et al.* 2016 Three-dimensional quantitative morphometric analysis (QMA) for *in situ* joint and tissue assessment of osteoarthritis in a preclinical rabbit disease model. *PLoS ONE* **11**, e0147564. (doi:10.1371/journal.pone.0147564)
75. Mittelstaedt D, Kahn D, Xia Y. 2016 Topographical and depth-dependent glycosaminoglycan concentration in canine medial tibial cartilage 3 weeks after anterior cruciate ligament transection surgery—a microscopic imaging study. *Quant. Imaging Med. Surg.* **6**, 648–660. (doi:10.21037/qims.2016.06.12)
76. Lakin BA, Patel H, Holland C, Freedman JD, Shelofsky JS, Snyder BD, Stok KS, Grinstaff MW. 2016 Contrast-enhanced CT using a cationic contrast agent enables non-destructive assessment of the biochemical and biomechanical properties of mouse tibial plateau cartilage. *J. Orthop. Res.* **34**, 1130–1138. (doi:10.1002/jor.23141)
77. Honkanen JTJ, Turunen MJ, Freedman JD, Saarakkala S, Grinstaff MW, Ylärinne JH, Jurvelin JS, Töyräs J. 2016 Cationic contrast agent diffusion differs between cartilage and meniscus. *Ann. Biomed. Eng.* **44**, 2913–2921. (doi:10.1007/s10439-016-1629-z)
78. Wang V *et al.* 2015 Assessment of glenoid chondral healing: comparison of microfracture to autologous matrix-induced chondrogenesis in a novel rabbit shoulder model. *J. Shoulder Elbow Surg.* **24**, 1789–1800. (doi:10.1016/j.jse.2015.06.008)
79. Nieminen H *et al.* 2015 Determining collagen distribution in articular cartilage using contrast-enhanced micro-computed tomography. *Osteoarthr. Cartil.* **23**, 1613–1621. (doi:10.1016/j.joca.2015.05.004)
80. Li XF, Cai XR, Fan F, Niu HJ, Li SY, Li DY, Fan YB, Qin YX. 2015 Observation of sGAG content of human hip joint cartilage in different old age groups based on EPIC micro-CT. *Connect. Tissue Res.* **56**, 99–105. (doi:10.3109/03008207.2015.1009052)
81. Lakin B, Ellis D, Shelofsky J, Freedman J, Grinstaff M, Snyder B. 2015 Contrast-enhanced CT facilitates rapid, non-destructive assessment of cartilage and bone properties of the human metacarpal. *Osteoarthr. Cartil.* **23**, 2158–2166. (doi:10.1016/j.joca.2015.05.033)
82. Fan F, Xiaofei L, Pengling R, Xiran C, Yan Y, Yubo F, Haijun N. 2015 Correlations between X-ray attenuation and GAG content of different cartilage layers based on contrast agent enhanced Micro-CT. In *Annual Int. Conf. of the IEEE Engineering in Medicine and Biology Society. IEEE Engineering in Medicine and Biology Society. Annual International Conference*, vol. 2015, pp. 6366–6369. IEEE. (doi:10.1109/EMBC.2015.7319849)
83. Bagi C, Zakur D, Berryman E, Andresen C, Wilkie D. 2015 Correlation between μCT imaging, histology and functional capacity of the osteoarthritic knee in the rat model of osteoarthritis. *J. Transl. Med.* **13**, 276. (doi:10.1186/s12967-015-0641-7)
84. Bagi C, Berryman E, Zakur D, Wilkie D, Andresen C. 2015 Effect of antiresorptive and anabolic bone therapy on development of osteoarthritis in a posttraumatic rat model of OA. *Arthritis Res. Ther.* **17**, 315. (doi:10.1186/s13075-015-0829-5)
85. Siebelt M, Waarsing J, Groen H, Müller C, Koelewijn S, de Blois E, Verhaar J, de Jong M, Weinans H. 2014 Inhibited osteoclastic bone resorption through alendronate treatment in rats reduces severe osteoarthritis progression. *Bone* **66**, 163–170. (doi:10.1016/j.bone.2014.06.009)
86. Siebelt M, Van der Windt A, Groen H, Sandker M, Waarsing J, Müller C, De Jong M, Jahr H, Weinans H. 2014 FK506 protects against articular cartilage collagenous extra-cellular matrix degradation. *Osteoarthr. Cartil.* **22**, 591–600. (doi:10.1016/j.joca.2014.02.003)
87. Renders G, Mulder L, Lin A, Langenbach G, Koolstra J, Guldberg R, Everts V. 2014 Contrast-enhanced microCT (EPIC-μCT) *ex vivo* applied to the mouse and human jaw joint. *Dentomaxillofac. Radiol.* **43**, 20130098. (doi:10.1259/dmfr.20130098)

88. Kerckhofs G, Sainz J, Maréchal M, Wevers M, Van de Putte T, Geris L, Schrooten J. 2014 Contrast-enhanced nanofocus X-ray computed tomography allows virtual three-dimensional histopathology and morphometric analysis of osteoarthritis in small animal models. *Cartilage* **5**, 55–65. (doi:10.1177/1947603513501175)
89. Fu M, Liu J, Huang G, Huang Z, Zhang Z, Wu P, Wang B, Yang Z, Liao W. 2014 Impaired ossification coupled with accelerated cartilage degeneration in developmental dysplasia of the hip: evidences from μCT arthrography in a rat model. *BMC Musculoskelet. Disord.* **15**, 339. (doi:10.1186/1471-2474-15-339)
90. Freedman J, Lusic H, Snyder B, Grinstaff M. 2014 Tantalum oxide nanoparticles for the imaging of articular cartilage using X-ray computed tomography: visualization of *ex vivo*/*in vivo* murine tibia and *ex vivo* human index finger cartilage. *Angew. Chem. Int. Ed.* **53**, 8406–8410. (doi:10.1002/anie.201404519)
91. Entezari V, Bansal P, Stewart R, Lakin B, Grinstaff M, Snyder B. 2014 Effect of mechanical convection on the partitioning of an anionic iodinated contrast agent in intact patellar cartilage. *J. Orthop. Res.* **32**, 1333–1340. (doi:10.1002/jor.22662)
92. Thote T, Lin A, Raji Y, Moran S, Stevens H, Hart M, Kamath R, Guldberg R, Willett N. 2013 Localized 3D analysis of cartilage composition and morphology in small animal models of joint degeneration. *Osteoarthr. Cartil.* **21**, 1132–1141. (doi:10.1016/j.joca.2013.05.018)
93. Stewart RC, Bansal PN, Entezari V, Lusic H, Nazarian RM, Snyder BD, Grinstaff MW. 2013 Contrast-enhanced CT with a high-affinity cationic contrast agent for imaging *ex vivo* bovine, intact *ex vivo* rabbit, and *in vivo* rabbit cartilage. *Radiology* **266**, 141–150. (doi:10.1148/radiol.12112246)
94. Lakin BA, Grasso DJ, Shah SS, Stewart RC, Bansal PN, Freedman JD, Grinstaff MW, Snyder BD. 2013 Cationic agent contrast-enhanced computed tomography imaging of cartilage correlates with the compressive modulus and coefficient of friction. *Osteoarthr. Cartil.* **21**, 60–68. (doi:10.1016/j.joca.2012.09.007)
95. Wang J, Gao Y, Hou Y, Zhao F, Pu F, Liu X, Wu Z, Fan Y. 2012 Evaluation on cartilage morphology after intraarticular injection of titanium dioxide nanoparticles in rats. *J. Nanomater.* **2012**, 452767. (doi:10.1155/2012/452767)
96. Van Tiel J *et al.* 2012 CT arthrography of the human knee to measure cartilage quality with low radiation dose. *Osteoarthr. Cartil.* **20**, 678–685. (doi:10.1016/j.joca.2012.03.007)
97. Kotwal N, Li J, Sandy J, Plaas A, Sumner D. 2012 Initial application of EPIC-μCT to assess mouse articular cartilage morphology and composition: effects of aging and treadmill running. *Osteoarthr. Cartil.* **20**, 887–895. (doi:10.1016/j.joca.2012.04.012)
98. Kerckhofs G, Sainz J, Wevers M, Van de Putte T, Schrooten J. 2012 Contrast-enhanced nanofocus computed tomography images the cartilage subtissue architecture in three dimensions. *Eur. Cells Mater.* **25**, 179–189. (doi:10.22203/eCM.v025a13)
99. Siebelt M, Waarsing JH, Kops N, Piscaer TM, Verhaar JAN, Oei EHG, Weinans H. 2011 Quantifying osteoarthritic cartilage changes accurately using in vivo microCT arthrography in three etiologically distinct rat models. *J. Orthop. Res.* **29**, 1788–1794. (doi:10.1002/jor.21444)
100. Siebelt M *et al.* 2011 Clinically applied CT arthrography to measure the sulphated glycosaminoglycan content of cartilage. *Osteoarthr. Cartil.* **19**, 1183–1189. (doi:10.1016/j.joca.2011.07.006)
101. Bansal P, Stewart R, Entezari V, Snyder B, Grinstaff M. 2011 Contrast agent electrostatic attraction rather than repulsion to glycosaminoglycans affords a greater contrast uptake ratio and improved quantitative CT imaging in cartilage. *Osteoarthr. Cartil.* **19**, 970–976. (doi:10.1016/j.joca.2011.04.004)
102. Bansal PN, Joshi NS, Entezari V, Malone BC, Stewart RC, Snyder BD, Grinstaff MW. 2011 Cationic contrast agents improve quantification of glycosaminoglycan (GAG) content by contrast enhanced CT imaging of cartilage. *J. Orthop. Res.* **29**, 704–709. (doi:10.1002/jor.21312)
103. Xie L, Lin A, Guldberg R, Levenston M. 2010 Nondestructive assessment of sGAG content and distribution in normal and degraded rat articular cartilage *via* EPIC-μCT. *Osteoarthr. Cartil.* **18**, 65–72. (doi:10.1016/j.joca.2009.07.014)
104. Bansal P, Joshi N, Entezari V, Grinstaff M, Snyder B. 2010 Contrast enhanced computed tomography can predict the glycosaminoglycan content and biomechanical properties of articular cartilage. *Osteoarthr. Cartil.* **18**, 184–191. (doi:10.1016/j.joca.2009.09.003)
105. Xie L, Lin A, Levenston M, Guldberg R. 2009 Quantitative assessment of articular cartilage morphology via EPIC-μCT. *Osteoarthr. Cartil.* **17**, 313–320. (doi:10.1016/j.joca.2008.07.015)

106. Taylor C, Carballido-Gamio J, Majumdar S, Li X. 2009 Comparison of quantitative imaging of cartilage for osteoarthritis: T2, T1 ρ, dGEMRIC and contrast-enhanced computed tomography. *Magn. Reson. Imaging* **27**, 779–784. (doi:10.1016/j.mri.2009.01.016)
107. Joshi NS, Bansal PN, Stewart RC, Snyder BD, Grinstaff MW. 2009 Effect of contrast agent charge on visualization of articular cartilage using computed tomography: exploiting electrostatic interactions for improved sensitivity. *J. Am. Chem. Soc.* **131**, 13 234–13 235. (doi:10.1021/ja9053306)
108. Piscaer TM, Waarsing JH, Kops N, Pavljasevic P, Verhaar JAN, van Osch GJVM, Weinans H. 2008 *In vivo* imaging of cartilage degeneration using μCT-arthrography. *Osteoarthr. Cartil.* **16**, 1011–1017. (doi:10.1016/j.joca.2008.01.012)
109. Palmer AW, Guldberg RE, Levenston ME. 2006 Analysis of cartilage matrix fixed charge density and three-dimensional morphology via contrast-enhanced microcomputed tomography. *Proc. Natl Acad. Sci. USA* **103**, 19 255–19 260. (doi:10.1073/pnas.0606406103)
110. Majda D, Bhattarai A, Riikonen J, Napruszewska B, Zimowska M, Michalik-Zym A, Ťyŕs J, Lehto VP. 2017 New approach for determining cartilage pore size distribution: NaCl-thermoporometry. *Microporous Mesoporous Mater.* **241**, 238–245. (doi:10.1016/j.micromeso.2017.01.005)
111. Nemetschek T, Riedl H, Jonak R. 1979 Topochemistry of the binding of phosphotungstic acid to collagen. *J. Mol. Biol.* **133**, 67–83. (doi:10.1016/0022-2836(79)90251-1)
112. Zhang C, Vedadghavami A, He T, Charles JF, Bajpayee AG. 2023 Cationic carrier mediated delivery of anionic contrast agents in low doses enable enhanced computed tomography imaging of cartilage for early osteoarthritis diagnosis. *ACS Nano* **17**, 6649–6663. (doi:10.1021/acsnano.2c12376)
113. Ojanen SP, Finnilä MAJ, Herzog W, Saarakkala S, Korhonen RK, Rieppo L. 2023 Micro-computed tomography-based collagen orientation and anisotropy analysis of rabbit articular cartilage. *Ann. Biomed. Eng.* **51**, 1769–1780. (doi:10.1007/s10439-023-03183-4)
114. Bhattarai A *et al.* 2018 Quantitative dual contrast CT technique for evaluation of articular cartilage properties. *Ann. Biomed. Eng.* **46**, 1038–1046. (doi:10.1007/s10439-018-2013-y)
115. Saukko AEA, Turunen MJ, Honkanen MKM, Lovric G, Tiitu V, Honkanen JTJ, Grinstaff MW, Jurvelin JS, Töyräs J. 2019 Simultaneous quantitation of cationic and non-ionic contrast agents in articular cartilage using synchrotron microCT imaging. *Sci. Rep.* **9**, 7118. (doi:10.1038/s41598-019-43276-6)
116. Bhattarai A *et al.* 2020 Dual contrast in computed tomography allows earlier characterization of articular cartilage over single contrast. *J. Orthop. Res.* **38**, 2230–2238. (doi:10.1002/jor.24774)
117. Honkanen MKM, Saukko AEA, Turunen MJ, Xu W, Lovric G, Honkanen JTJ, Grinstaff MW, Lehto VP, Töyräs J. 2020 Triple contrast CT method enables simultaneous evaluation of articular cartilage composition and segmentation. *Ann. Biomed. Eng.* **48**, 556–567. (doi:10.1007/s10439-019-02362-6)
118. Honkanen MKM *et al.* 2020 Synchrotron microCT reveals the potential of the dual contrast technique for quantitative assessment of human articular cartilage composition. *J. Orthop. Res.* **38**, 563–573. (doi:10.1002/jor.24479)
119. Bhattarai A, Mäkelä JTA, Pouran B, Kröger H, Weinans H, Grinstaff MW, Töyräs J, Turunen MJ. 2021 Effects of human articular cartilage constituents on simultaneous diffusion of cationic and nonionic contrast agents. *J. Orthop. Res.* **39**, 771–779. (doi:10.1002/jor.24824)
120. Saukko AEA *et al.* 2022 Dualcontrast computed tomography enables detection of equine posttraumatic osteoarthritis in vitro. *J. Orthop. Res.* **40**, 703–711. (doi:10.1002/jor.25066)
121. Hsu JC, Nieves LM, Betzer O, Sadan T, Noël PB, Popovtzer R, Cormode DP. 2020 Nanoparticle contrast agents for Xray imaging applications. *Wiley Interdiscip. Rev. Nanomed. Nanobiotechnol.* **12**, e1642. (doi:10.1002/wnan.1642)
122. Pedersen DR, Goetz JE, Kurriger GL, Martin JA. 2013 Comparative digital cartilage histology for human and common osteoarthritis models. *Orthop. Res. Rev.* **2013**, 13–20. (doi:10.2147/ORR.S38400)
123. Alvarez RE, Macovski A. 1976 Energy-selective reconstructions in X-ray computerised tomography. *Phys. Med. Biol.* **21**, 733–744. (doi:10.1088/0031-9155/21/5/002)
124. Lehmann LA, Alvarez RE, Macovski A, Brody WR, Pelc NJ, Riederer SJ, Hall AL. 1981 Generalized image combinations in dual KVP digital radiography. *Med. Phys.* **8**, 659–667. (doi:10.1118/1.595025)
125. Thomlinson W, Elleaume H, Porra L, Suortti P. 2018 K-edge subtraction synchrotron X-ray imaging in bio-medical research. *Phys. Med.* **49**, 58–76. (doi:10.1016/j.ejmp.2018.04.389)

126. Perion P, Brombal L, Delogu P, Di Trapani V, Menk RH, Oliva P, Arfelli F. 2024 A high sensitivity wide bandwidth spectral system for multiple K-edge imaging. *J. Phys. D: Appl. Phys.* **57**, 355402. (doi:10.1088/1361-6463/ad4f9b)
127. Kulpe S *et al.* 2019 K-edge subtraction computed tomography with a compact synchrotron X-ray source. *Sci. Rep.* **9**, 13332. (doi:10.1038/s41598-019-49899-z)
128. Honkanen MKM, Matikka H, Honkanen JTJ, Bhattarai A, Grinstaff MW, Joukainen A, Kröger H, Jurvelin JS, Töyräs J. 2019 Imaging of proteoglycan and water contents in human articular cartilage with full-body CT using dual contrast technique. *J. Orthop. Res.* **37**, 1059–1070. (doi:10.1002/jor.24256)
129. Paakkari P *et al.* 2021 Quantitative dual contrast photon-counting computed tomography for assessment of articular cartilage health. *Sci. Rep.* **11**, 5556. (doi:10.1038/s41598-021-84800-x)
130. Flohr T, Petersilka M, Henning A, Ulzheimer S, Ferda J, Schmidt B. 2020 Photon-counting CT review. *Phys. Med.* **79**, 126–136. (doi:10.1016/j.ejmp.2020.10.030)
131. Taguchi K, Iwanczyk JS. 2013 Vision 20/20: single photon counting X-ray detectors in medical imaging: vision 20/20: photon counting detectors. *Med. Phys.* **40**, 100901. (doi:10.1118/1.4820371)
132. Rajendran K, Baffour F, Powell G, Glazebrook K, Thorne J, Larson N, Leng S, McCollough C, Fletcher J. 2023 Improved visualization of the wrist at lower radiation dose with photon-counting-detector CT. *Skeletal Radiol.* **52**, 23–29. (doi:10.1007/s00256-022-04117-2)
133. Fantoni S, Brun F, Cardarelli P, Baruffaldi F, Cristofori V, Taibi A, Trapella C, Brombal L. 2024 Quantitative spectral micro-CT of a CA4+ loaded osteochondral sample with a tabletop system. *Eur. Phys. J. Plus* **139**, 735. (doi:10.1140/epjp/s13360-024-05428-0)
134. Rajendran K *et al.* 2022 First clinical photon-counting detector CT system: technical evaluation. *Radiology* **303**, 130–138. (doi:10.1148/radiol.212579)
135. Brombal L, Arfelli F, Menk RH, Rigon L, Brun F. 2023 PEPI Lab: a flexible compact multi-modal setup for X-ray phase-contrast and spectral imaging. *Sci. Rep.* **13**, 4206. (doi:10.1038/s41598-023-30316-5)
136. Luetkens KS *et al.* 2023 Ultra-high-resolution photon-counting detector CT arthrography of the ankle: a feasibility study. *Diagnostics* **13**, 2201. (doi:10.3390/diagnostics13132201)
137. Kim DY, Yoon JM, Park G, Kang H, Lee DO, Lee D. 2023 Computed tomography arthrography versus magnetic resonance imaging for diagnosis of osteochondral lesions of the talus. *Arch. Orthop. Trauma Surg.* **143**, 5631–5639. (doi:10.1007/s00402-023-04871-5)
138. Paakkari P *et al.* 2023 Tantalum and iodine based dual-contrast photon-counting computed tomography method for assessment of articular cartilage composition. *Osteoarthr. Cartil.* **31**, S273. (doi:10.1016/j.joca.2023.01.278)
139. Tuppurainen J *et al.* 2024 Revealing detailed cartilage function through nanoparticle diffusion imaging: a computed tomography & finite element study. *Ann. Biomed. Eng.* **52**, 2584–2595. (doi:10.1007/s10439-024-03552-7)
140. Rajendran K *et al.* 2017 Quantitative imaging of excised osteoarthritic cartilage using spectral CT. *Eur. Radiol.* **27**, 384–392. (doi:10.1007/s00330-016-4374-7)
141. Baer K *et al.* 2021 Spectral CT imaging of human osteoarthritic cartilage via quantitative assessment of glycosaminoglycan content using multiple contrast agents. *APL Bioeng.* **5**, 026101. (doi:10.1063/5.0035312)
142. Zhou SA, Brahme A. 2008 Development of phase-contrast X-ray imaging techniques and potential medical applications. *Phys. Med.* **24**, 129–148. (doi:10.1016/j.ejmp.2008.05.006)
143. Momose A, Takeda T, Itai Y. 2000 Blood vessels: depiction at phase-contrast X-ray imaging without contrast agents in the mouse and rat—feasibility study. *Radiology* **217**, 593–596. (doi:10.1148/radiology.217.2.r00oc14593)
144. Peterzol A, Olivo A, Rigon L, Pani S, Dreossi D. 2005 The effects of the imaging system on the validity limits of the rayoptical approach to phase contrast imaging. *Med. Phys.* **32**, 3617–3627. (doi:10.1118/1.2126207)
145. Cloetens P, Barrett R, Baruchel J, Guigay JP, Schlenker M. 1996 Phase objects in synchrotron radiation hard X-ray imaging. *J. Phys. D: Appl. Phys.* **29**, 133–146. (doi:10.1088/0022-3727/29/1/023)
146. Momose A, Takeda T, Itai Y, Hirano K. 1996 Phase–contrast X-ray computed tomography for observing biological soft tissues. *Nat. Med.* **2**, 473–475. (doi:10.1038/nm0496-473)
147. Snigirev A, Snigireva I, Kohn V, Kuznetsov S, Schelokov I. 1995 On the possibilities of X-ray phase contrast microimaging by coherent highenergy synchrotron radiation. *Rev. Sci. Instrum.* **66**, 5486–5492. (doi:10.1063/1.1146073)

148. Pfeiffer F, Weitkamp T, Bunk O, David C. 2006 Phase retrieval and differential phase-contrast imaging with low-brilliance X-ray sources. *Nat. Phys.* **2**, 258–261. (doi:10.1038/nphys265)
149. Olivo A, Speller R. 2007 A coded-aperture technique allowing X-ray phase contrast imaging with conventional sources. *Appl. Phys. Lett.* **91**, 074106. (doi:10.1063/1.2772193)
150. Wilkins SW, Gureyev TE, Gao D, Pogany A, Stevenson AW. 1996 Phase-contrast imaging using polychromatic hard X-rays. *Nature* **384**, 335–338. (doi:10.1038/384335a0)
151. Ikeura-Sekiguchi H *et al.* 2008 In-line phase-contrast imaging of a biological specimen using a compact laser-Compton scattering-based X-ray source. *Appl. Phys. Lett.* **92**, 131107. (doi:10.1063/1.2903148)
152. Dejea H, Pierantoni M, Orozco GA, Gstöhl SJ, Schlepütz CM, Isaksson H. 2024 *In situ* loading and timeresolved synchrotronbased phase contrast tomography for the mechanical investigation of connective knee tissues: a proof-of-concept study. *Adv. Sci.* **11**, 2308811. (doi:10.1002/advs.202308811)
153. Bissardon C, Zhang Y, Labriet H, Berujon S, Charlet L, Khan I, Brun E, Bohic S. 2022 *In vitro* preparation of actively maturing bovine articular cartilage explants for X-ray phase contrast imaging. *J. Vis. Exp.* **179**, e61607. (doi:10.3791/61607)
154. Horng A *et al.* 2021 Multiscale X-ray phase contrast imaging of human cartilage for investigating osteoarthritis formation. *J. Biomed. Sci.* **28**, 42. (doi:10.1186/s12929-021-00739-1)
155. Broche L, Favier B, Rougé-Labriet H, Drevet S, Lardy B, Brun E, Lemasson B. 2021 Calcified cartilage revealed in whole joint by X-ray phase contrast imaging. *Osteoarthr. Cartil. Open* **3**, 100168. (doi:10.1016/j.ocarto.2021.100168)
156. Tozzi G, Fernández M, Davis S, Karali A, Kao A, Blunn G. 2020 Full-field strain uncertainties and residuals at the cartilage-bone interface in unstained tissues using propagation-based phase-contrast XCT and digital volume correlation. *Materials* **13**, 2579. (doi:10.3390/ma13112579)
157. Rack A, Stroebel J, Rack T, Dabin Y, Knabe C, Stiller M, Coan P, Bleuet P. 2020 TomoPress—in situ synchrotron-based microtomography under axial load. *Instruments* **4**, 11. (doi:10.3390/instruments4020011)
158. Madi K, Staines K, Bay B, Javaheri B, Geng H, Bodey A, Cartmell S, Pitsillides A, Lee P. 2020 In situ characterization of nanoscale strains in loaded whole joints via synchrotron X-ray tomography. *Nat. Biomed. Eng.* **4**, 343–354. (doi:10.1038/s41551-019-0477-1)
159. Geith T *et al.* 2018 Quantitative assessment of degenerative cartilage and subchondral bony lesions in a preserved cadaveric knee: propagation-based phase-contrast CT versus conventional MRI and CT. *Am. J. Roentgenol.* **210**, 1317–1322. (doi:10.2214/AJR.17.18286)
160. Yoon J, Won S, Kim S, Hong S, Kim G, Kim J. 2015 Phase-contrast radiography enables detection of early changes in articular cartilage in a mouse model of osteoarthritis. *Am. J. Phys. Med. Rehabil.* **94**, 644–648. (doi:10.1097/PHM.0000000000000232)
161. Sun W, Zhang Y, Gao F, Li Z, Li G, Pan L. 2015 Phase-contrast imaging with synchrotron hard X-ray of micro lesions of the cartilage of the femoral head in rabbits. *Int. J. Clin. Exp. Med.* **8**, 20 086–20 091.
162. Li J, Yuan H, Wu M, Dong L, Zhang L, Shi H, Luo S. 2014 Quantitative assessment of murine articular cartilage and bone using X-ray phase-contrast imaging. *PLoS ONE* **9**, e111939. (doi:10.1371/journal.pone.0111939)
163. Horng A *et al.* 2014 Cartilage and soft tissue imaging using X-rays: propagation-based phase-contrast computed tomography of the human knee in comparison with clinical imaging techniques and histology. *Invest. Radiol.* **49**, 627–634. (doi:10.1097/RLI.0000000000000063)
164. Zehbe R, Riesemeier H, Kirkpatrick C, Brochhausen C. 2012 Imaging of articular cartilage—data matching using X-ray tomography, SEM, FIB slicing and conventional histology. *Micron* **43**, 1060–1067. (doi:10.1016/j.micron.2012.05.001)
165. Lee Y *et al.* 2010 Articular cartilage imaging by the use of phase-contrast tomography in a collagen-induced arthritis mouse model. *Acad. Radiol.* **17**, 244–250. (doi:10.1016/j.acra.2009.09.015)
166. Ismail E, Kaabar W, Garrity D, Gundogdu O, Bunk O, Pfeiffer F, Farquharson M, Bradley D. 2010 X-ray phase contrast imaging of the bone-cartilage interface. *Appl. Radiat. Isot.* **68**, 767–771. (doi:10.1016/j.apradiso.2009.09.042)
167. Choi CH, Kim HT, Choe JY, Kim SK, Choi GW, Jheon S, Kim JK. 2010 *In vivo* high-resolution synchrotron radiation imaging of collagen-induced arthritis in a rodent model. *J. Synchrotron Radiat.* **17**, 393–399. (doi:10.1107/S0909049510009581)

168. Shimao D, Mori K, Sigiyama H, Hyodo K. 2005 Refraction-contrast articular cartilage image: comparison of depiction abilities between in-line holographic method and a Laue type analyzer method. *Jpn. J. Appl. Phys. Part 1: Regul. Pap. Short Notes Rev. Pap.* **44**, 450–451. (doi:10.1143/JJAP.44.450)
169. Brombal L *et al.* 2018 Phase-contrast breast CT: the effect of propagation distance. *Phys. Med. Biol.* **63**, 24NT03. (doi:10.1088/1361-6560/aaf2e1)
170. Gureyev TE, Nesterets YI, Kozlov A, Paganin DM, Quiney HM. 2017 On the "unreasonable" effectiveness of transport of intensity imaging and optical deconvolution. *J. Opt. Soc. Am. A* **34**, 2251. (doi:10.1364/JOSAA.34.002251)
171. Ruan M, Dawson B, Jiang MM, Gannon F, Heggeness M, Lee B. 2013 Quantitative imaging of murine osteoarthritic cartilage by phase-contrast micro-computed tomography. *Arthritis Rheum.* **65**, 388–396. (doi:10.1002/art.37766)
172. Clark J *et al.* 2020 Exploratory full-field mechanical analysis across the osteochondral tissue—biomaterial interface in an ovine model. *Materials* **13**, 3911. (doi:10.3390/ma13183911)
173. Jayaram P, Liu C, Dawson B, Ketkar S, Patel S, Lee B, Grol M. 2020 Leukocyte-dependent effects of platelet-rich plasma on cartilage loss and thermal hyperalgesia in a mouse model of post-traumatic osteoarthritis. *Osteoarthr. Cartil.* **28**, 1385–1393. (doi:10.1016/j.joca.2020.06.004)
174. Stone A *et al.* 2019 Combinatorial *Prg4* and *Il-1ra* gene therapy protects against hyperalgesia and cartilage degeneration in post-traumatic osteoarthritis. *Hum. Gene Ther.* **30**, 225–235. (doi:10.1089/hum.2018.106)
175. Nixon AJ *et al.* 2018 Diseasemodifying osteoarthritis treatment with interleukin-1 receptor antagonist gene therapy in small and large animal models. *Arthritis Rheumatol.* **70**, 1757–1768. (doi:10.1002/art.40668)
176. Ruan MZC *et al.* 2013 Proteoglycan 4 expression protects against the development of osteoarthritis. *Sci. Transl. Med.* **5**, 176ra34. (doi:10.1126/scitranslmed.3005409)
177. Ruan M, Patel R, Dawson B, Jiang MM, Lee B. 2013 Pain, motor and gait assessment of murine osteoarthritis in a cruciate ligament transection model. *Osteoarthr. Cartil.* **21**, 1355–1364. (doi:10.1016/j.joca.2013.06.016)
178. Cloetens P, Ludwig W, Baruchel J, Van Dyck D, Van Landuyt J, Guigay JP, Schlenker M. 1999 Holotomography: quantitative phase tomography with micrometer resolution using hard synchrotron radiation X rays. *Appl. Phys. Lett.* **75**, 2912–2914. (doi:10.1063/1.125225)
179. Paganin D, Mayo SC, Gureyev TE, Miller PR, Wilkins SW. 2002 Simultaneous phase and amplitude extraction from a single defocused image of a homogeneous object. *J. Microsc.* **206**, 33–40. (doi:10.1046/j.1365-2818.2002.01010.x)
180. Ingal VN, Beliaevskaya EA. 1995 X-ray plane-wave topography observation of the phase contrast from a non-crystalline object. *J. Phys. D: Appl. Phys.* **28**, 2314–2317. (doi:10.1088/0022-3727/28/11/012)
181. Davis TJ, Gao D, Gureyev TE, Stevenson AW, Wilkins SW. 1995 Phase-contrast imaging of weakly absorbing materials using hard X-rays. *Nature* **373**, 595–598. (doi:10.1038/373595a0)
182. Chapman D *et al.* 1997 Diffraction enhanced x-ray imaging. *Phys. Med. Biol.* **42**, 2015–2025. (doi:10.1088/0031-9155/42/11/001)
183. Talbot H. 1836 LXXVI. Facts relating to optical science. No. IV. *Lond. Edinb. Dublin Philos. Mag. J. Sci.* **9**, 401–407. (doi:10.1080/14786443608649032)
184. Nagarajan M, Coan P, Huber M, Diemoz P, Wismüller A. 2015 Integrating dimension reduction and out-of-sample extension in automated classification of ex vivo human patellar cartilage on phase contrast X-ray computed tomography. *PLoS ONE* **10**, e0117157. (doi:10.1371/journal.pone.0117157)
185. Crittell S, Cheung KC, Hall C, Ibison M, Nolan P, Page R, Scraggs D, Wilkinson S. 2007 Diffraction enhanced imaging of normal and arthritic mice feet. *Nucl. Instrum. Methods Phys. Res. A* **573**, 126–128. (doi:10.1016/j.nima.2006.11.044)
186. Li J, Wilson N, Zelazny A, Meyer J, Zhong Z, Muehleman C. 2013 Assessment of diffraction-enhanced synchrotron imaging for cartilage degeneration of the human knee joint. *Clin. Anat.* **26**, 621–629. (doi:10.1002/ca.22106)
187. Muehleman C, Li J, Zhong Z. 2006 Preliminary study on diffraction enhanced radiographic imaging for a canine model of cartilage damage. *Osteoarthr. Cartil.* **14**, 882–888. (doi:10.1016/j.joca.2006.02.011)

188. Miki H, Hirano K, Ninomiya T, Arai Y, Honda K. 2023 Visualization of temporomandibular joint articular cartilage using synchrotron-radiation X-ray phase-contrast imaging. *Nucl. Instrum. Methods Phys. Res., Sect. A* **1049**, 168005. (doi:10.1016/j.nima.2022.168005)
189. Wagner A *et al.* 2005 Chance and limit of imaging of articular cartilage in vitro in healthy and arthritic joints—DEI (Diffraction Enhanced Imaging) in comparison with MRI, CT and ultrasound. *Medical imaging 2005: physiology, function, and structure from medical images, PTS 1 and 2*, vol. 5746, pp. 542–549. Eisenberg, Germany: Univ. Jena, Dept. Orthopaed., Rudolf Elle Hosp Eisenberg, D-07607. (doi:10.1117/12.589614)
190. Li J, Williams JM, Zhong Z, Kuettner KE, Aurich M, Mollenhauer J, Muehleman C. 2005 Reliability of diffraction enhanced imaging for assessment of cartilage lesions, *ex vivo*. *Osteoarthr. Cartil.* **13**, 187–197. (doi:10.1016/j.joca.2004.11.003)
191. Mollenhauer J *et al.* 2002 Diffraction-enhanced X-ray imaging of articular cartilage. *Osteoarthr. Cartil.* **10**, 163–171. (doi:10.1053/joca.2001.0496)
192. Li J, Zhong Z, Lidtke R, Kuettner K, Peterfy C, Aliyeva E, Muehleman C. 2003 Radiography of soft tissue of the foot and ankle with diffraction enhanced imaging. *J. Anat.* **202**, 463–470. (doi:10.1046/j.1469-7580.2003.00175.x)
193. Muehleman C, Chapman L, Kuettner K, Rieff J, Mollenhauer J, Massuda K, Zhong Z. 2003 Radiography of rabbit articular cartilage with diffraction-enhanced imaging. *Anat. Rec. A, Discov. Mol. Cell. Evol. Biol.* **272**, 392–397. (doi:10.1002/ar.a.10043)
194. Majumdar S, Issever A, Burghardt A, Lotz J, Arfelli F, Rigon L, Heitner G, Menk RH. 2004 Diffraction enhanced imaging of articular cartilage and comparison with micro-computed tomography of the underlying bone structure. *Eur. Radiol.* **14**, 1440–1448. (doi:10.1007/s00330-004-2355-8)
195. Muehleman C, Li J, Wernick M, Brankov J, Kuettner K, Zhong Z. 2004 Yes, you can see cartilage with X-rays; diffraction enhanced X-ray imaging for soft and hard tissues. *J. Musculoskelet. Neuronal Interact.* **4**, 369–370.
196. Shimao D, Mori K, Hyodo K, Sugiyama H, Ando M. 2004 Application of X-ray refraction-contrast to medical joint imaging. *Synchrotron Radiat. Instrum.* **705**, 1324–1327. (doi:10.1063/1.1758045)
197. Abidin A, Deng B, DSouza A, Nagarajan M, Coan P, Wismüller A. 2018 Deep transfer learning for characterizing chondrocyte patterns in phase contrast X-Ray computed tomography images of the human patellar cartilage. *Comput. Biol. Med.* **95**, 24–33. (doi:10.1016/j.compbiomed.2018.01.008)
198. Gasilov S, Mittone A, Horng A, Geith T, Bravin A, Baumbach T, Coan P. 2016 Hard X-ray index of refraction tomography of a whole rabbit knee joint: a feasibility study. *Phys. Med.* **32**, 1785–1789. (doi:10.1016/j.ejmp.2016.10.001)
199. Rhoades G, Belev G, Chapman L, Wiebe S, Cooper D, Wong A, Rosenberg A. 2015 Diffraction-enhanced computed tomographic imaging of growing piglet joints by using a synchrotron light source. *Comp. Med.* **65**, 342–347.
200. Nagarajan M, Coan P, Huber M, Diemoz P, Wismüller A. 2015 Volumetric quantitative characterization of human patellar cartilage with topological and geometrical features on phase-contrast X-ray computed tomography. *Med. Biol. Eng. Comput.* **53**, 1211–1220. (doi:10.1007/s11517-015-1340-5)
201. Majidi K, Wernick M, Li J, Muehleman C, Brankov J. 2014 Limited-angle tomography for analyzer-based phase-contrast X-ray imaging. *Phys. Med. Biol.* **59**, 3483–3500. (doi:10.1088/0031-9155/59/13/3483)
202. Fogarty D, Reinhart B, Tzvetkov T, Nesch I, Williams C. 2011 In-laboratory diffraction-enhanced X-ray imaging of an equine hoof. *J. Equine Vet. Sci.* **31**, 365–369. (doi:10.1016/j.jevs.2011.03.015)
203. Muehleman C, Fogarty D, Reinhart B, Tzvetkov T, Li J, Nesch I. 2010 In-laboratory diffraction-enhanced X-ray imaging for articular cartilage. *Clin. Anat.* **23**, 530–538. (doi:10.1002/ca.20993)
204. Diemoz PC, Coan P, Glaser C, Bravin A. 2010 Absorption, refraction and scattering in analyzer-based imaging: comparison of different algorithms. *Opt. Express* **18**, 3494–3509. (doi:10.1364/OE.18.003494)
205. Diemoz P, Bravin A, Glaser C, Coan P. 2010 Comparison of analyzer-based imaging computed tomography extraction algorithms and application to bone-cartilage imaging. *Phys. Med. Biol.* **55**, 7663–7679. (doi:10.1088/0031-9155/55/24/018)

206. Coan P, Wagner A, Bravin A, Diemoz PC, Keyrilainen J, Mollenhauer J. 2010 *In vivo* x-ray phase contrast analyzer-based imaging for longitudinal osteoarthritis studies in guinea pigs. *Phys. Med. Biol.* **55**, 7649–7662. (doi:10.1088/0031-9155/55/24/017)
207. Coan P *et al.* 2010 Characterization of osteoarthritic and normal human patella cartilage by computed tomography X-ray phase-contrast imaging: a feasibility study. *Invest. Radiol.* **45**, 437–444. (doi:10.1097/RLI.0b013e3181e193bd)
208. Muehleman C, Li J, Connor D, Parham C, Pisano E, Zhong Z. 2009 Diffraction-enhanced imaging of musculoskeletal tissues using a conventional X-ray tube. *Acad. Radiol.* **16**, 918–923. (doi:10.1016/j.acra.2009.04.006)
209. Li J, Zhong Z, Connor D, Mollenhauer J, Muehleman C. 2009 Phase-sensitive X-ray imaging of synovial joints. *Osteoarthr. Cartil.* **17**, 1193–1196. (doi:10.1016/j.joca.2009.03.005)
210. Issever A, Diederichs G, Majumdar S, Rogalla P, Hamm B, Lange A, Harwardt M, Hentschel M, Mueller B. 2008 Analyser-based tomography images of cartilage. *J. Synchrotron Radiat.* **15**, 525–527. (doi:10.1107/S0909049508014829)
211. Muehleman C, Li J, Zhong Z, Brankov J, Wernick M. 2006 Multiple-image radiography for human soft tissue. *J. Anat.* **208**, 115–124. (doi:10.1111/j.1469-7580.2006.00502.x)
212. Wagner A *et al.* 2005 Options and limitations of joint cartilage imaging: DEI in comparison to MRI and sonography. *Nucl. Instrum. Methods Phys. Res. A* **548**, 47–53. (doi:10.1016/j.nima.2005.03.064)
213. Muehleman C *et al.* 2004 X-ray detection of structural orientation in human articular cartilage. *Osteoarthr. Cartil.* **12**, 97–105. (doi:10.1016/j.joca.2003.10.001)
214. David C, Nöhammer B, Solak HH, Ziegler E. 2002 Differential X-ray phase contrast imaging using a shearing interferometer. *Appl. Phys. Lett.* **81**, 3287–3289. (doi:10.1063/1.1516611)
215. Momose A, Kawamoto S, Koyama I, Hamaishi Y, Takai K, Suzuki Y. 2003 Demonstration of X-ray Talbot interferometry. *Jpn. J. Appl. Phys.* **42**, L866–L868. (doi:10.1143/JJAP.42.L866)
216. Brombal L, Rigon L. 2023 In *Hybrid imaging detectors in X-ray phase-contrast applications*, pp. 51–74. Switzerland: Springer International Publishing. (doi:10.1007/978-3-030-92989-3_3)
217. Pfeiffer F, Bech M, Bunk O, Kraft P, Eikenberry EF, Brönnimann C, Grünzweig C, David C. 2008 Hard-X-ray dark-field imaging using a grating interferometer. *Nat. Mater.* **7**, 134–137. (doi:10.1038/nmat2096)
218. Schulz G, Gotz C, Muller-Gerbl M, Zanette I, Zdora MC, Khimchenko A, Deyhle H, Thalmann P, Mueller B. 2017 Multimodal imaging of the human knee down to the cellular level. In *X-ray microscopy conference 2016 (XRM 2016)*, vol. 849. IOP Publishing. (doi:10.1088/1742-6596/849/1/012026)
219. Tada T, Murakoshi D, Ishii H, Hashimoto A, Kaneko Y, Ito W, Agano T. 2012 Fabrication of high aspect grating using bonded substrate for X-ray refraction imaging by Talbot-Lau interferometer. In *International workshop on X-Ray and neutron phase imaging with gratings*, vol. 1466, pp. 181–186. American Institute of Physics. (doi:10.1063/1.4742289)
220. Murakoshi D, Tada T, Ishii H, Hashimoto A, Kaneko Y, Ito W, Agano T. 2012 Feasibility study of the sub-pixel scanning method for single-exposure X-ray refraction imaging by Talbot-Lau interferometer using an a-Se direct conversion type FPD. In *Medical imaging 2012: physics of medical imaging*, vol. 8313. Society of Photo-Optical Instrumentation Engineers (SPIE). (doi:10.1117/12.910886)
221. Itoh H *et al.* 2011 Two-dimensional grating-based X-ray phase-contrast imaging using Fourier transform phase retrieval. *Opt. Express* **19**, 3339–3346. (doi:10.1364/OE.19.003339)
222. Makifuchi C, Kido K, Kiyohara J, Ito T, Nagatsuka S, Momose A. 2010 Development of X-Ray Talbot-Lau interferometer with a practical X-ray tube for medical imaging. In *Int. Conf. on Advanced Phase Measurement Methods in Optics an Imaging*, vol. 1236, p. 203. American Institute of Physics. (doi:10.1063/1.3426112)
223. Kido K, Makifuchi C, Kiyohara J, Itou T, Honda C, Momose A. 2010 Bone cartilage imaging with X-ray interferometry using a practical X-ray tube. In *Medical imaging 2010: physics of medical imaging*, vol. 7622. Society of Photo-Optical Instrumentation Engineers (SPIE). (doi:10.1117/12.843655)
224. Momose A, Yashiro W, Kuwabara H, Kawabata K. 2009 Grating-based X-ray phase imaging using multiline X-ray source. *Jpn. J. Appl. Phys.* **48**, 076512. (doi:10.1143/JJAP.48.076512)
225. Kawano S, Hoshino M, Matsumoto T. 2022 In-situ deformation imaging of articular cartilage using grating-based phase-contrast X-ray CT at a synchrotron light source. *J. Biorheol.* **36**, 51–57. (doi:10.17106/jbr.36.51)

226. Yoshioka H *et al.* 2020 Imaging evaluation of the cartilage in rheumatoid arthritis patients with an X-ray phase imaging apparatus based on Talbot-Lau interferometry. *Sci. Rep.* **10**, 6561. (doi:10.1038/s41598-020-63155-9)
227. Herzen J *et al.* 2019 3D grating-based X-ray phase-contrast computed tomography for high-resolution quantitative assessment of cartilage: an experimental feasibility study with 3T MRI, 7T MRI and biomechanical correlation. *PLoS ONE* **14**, e0212106. (doi:10.1371/journal.pone.0212106)
228. Khimchenko A, Schulz G, Thalmann P, Müller B. 2018 Implementation of a double-grating interferometer for phase-contrast computed tomography in a conventional system nanotomő m. *APL Bioeng.* **2**, 016106. (doi:10.1063/1.5022184)
229. Schulz G *et al.* 2016 Hierarchical imaging of the human knee. In *Developments in X-ray tomography X*, vol. 9967. Society of Photo-Optical Instrumentation Engineers (SPIE). (doi:10.1117/12.2238089)
230. Nagashima M, Tanaka J, Kiyohara J, Makifuchi C, Kido K, Momose A. 2014 Application of X-ray grating interferometry for the imaging of joint structures. *Anat. Sci. Int.* **89**, 95–100. (doi:10.1007/s12565-013-0204-z)
231. Momose A *et al.* 2014 X-ray phase imaging: from synchrotron to hospital. *Phil. Trans. R. Soc. A* **372**, 20130023. (doi:10.1098/rsta.2013.0023)
232. Tanaka J, Nagashima M, Kido K, Hoshino Y, Kiyohara J, Makifuchi C, Nishino S, Nagatsuka S, Momose A. 2013 Cadaveric and in vivo human joint imaging based on differential phase contrast by X-ray Talbot-Lau interferometry. *Z. Med. Phys.* **23**, 222–227. (doi:10.1016/j.zemedi.2012.11.004)
233. Kiyohara J *et al.* 2012 Development of the Talbot-Lau interferometry system available for clinical use. In *International workshop on X-ray and neutron phase imaging with gratings*, vol. 1466, pp. 97–102. American Institute of Physics. (doi:10.1063/1.4742275)
234. Diemoz P, Coan P, Zanette I, Bravin A, Lang S, Glaser C, Weitkamp T. 2011 A simplified approach for computed tomography with an X-ray grating interferometer. *Opt. Express* **19**, 1691–1698. (doi:10.1364/OE.19.001691)
235. Stutman D, TJ B, JA C, CO B. 2011 Talbot phase-contrast X-ray imaging for the small joints of the hand. *Phys. Med. Biol.* **56**, 5697–720. (doi:10.1088/0031-9155/56/17/015)
236. Marenzana M *et al.* 2014 Synchrotron- and laboratory-based X-ray phase-contrast imaging for imaging mouse articular cartilage in the absence of radiopaque contrast agents. *Phil. Trans. R. Soc. A* **372**, 20130127. (doi:10.1098/rsta.2013.0127)
237. Endrizzi M, Diemoz PC, Millard TP, Louise Jones J, Speller RD, Robinson IK, Olivo A. 2014 Hard X-ray dark-field imaging with incoherent sample illumination. *Appl. Phys. Lett.* **104**, 024106. (doi:10.1063/1.4861855)
238. Massimi L, Kallon G, Buchanan I, Endrizzi M, Dobrosz P, Brooks R, Brau D, Bullard E, Olivo A. 2022 Replacing the detector mask with a structured scintillator in edge-illumination X-ray phase contrast imaging. *J. Appl. Phys.* **131**, 204501. (doi:10.1063/5.0090139)
239. Endrizzi M *et al.* 2013 Edge illumination and coded-aperture X-ray phase-contrast imaging: increased sensitivity at synchrotrons and lab-based translations into medicine, biology and materials science. In *Medical imaging 2013: physics of medical imaging*, vol. 8668. Society of Photo-Optical Instrumentation Engineers (SPIE). (doi:10.1117/12.2007893)
240. Marenzana M, Hagen C, Borges P, Endrizzi M, Szafraniec M, Ignatyev K, Olivo A. 2012 Visualization of small lesions in rat cartilage by means of laboratory-based X-ray phase contrast imaging. *Phys. Med. Biol.* **57**, 8173–8184. (doi:10.1088/0031-9155/57/24/8173)
241. Diemoz P, Endrizzi M, Hagen C, Millard T, Vittoria F, Olivo A. 2015 Angular sensitivity and spatial resolution in edge illumination X-ray phase-contrast imaging. *Nucl. Instrum. Methods Phys. Res., Sect. A* **784**, 538–541. (doi:10.1016/j.nima.2014.12.027)
242. Olivo A *et al.* 2001 An innovative digital imaging set-up allowing a low-dose approach to phase contrast applications in the medical field. *Med. Phys.* **28**, 1610–1619. (doi:10.1118/1.1388219)
243. Kunisada T, Shimao D, Sugiyama H, Takeda K, Ozaki T, Ando M. 2008 X-ray dark field imaging of human articular cartilage: possible clinical application to orthopedic surgery. *Eur. J. Radiol.* **68**, S18–S21. (doi:10.1016/j.ejrad.2008.04.034)
244. Zanette I, Bech M, Rack A, Le Duc G, Tafforeau P, David C, Mohr J, Pfeiffer F, Weitkamp T. 2012 Trimodal low-dose X-ray tomography. *Proc. Natl Acad. Sci. USA* **109**, 10 199–10 204. (doi:10.1073/pnas.1117861109)

245. Rigon L, Arfelli F, Menk RH. 2007 Three-image diffraction enhanced imaging algorithm to extract absorption, refraction, and ultrasmall-angle scattering. *Appl. Phys. Lett.* **90**, 114102. (doi:10.1063/1.2713147)
246. Ando M *et al.* 2016 Dark-field imaging: recent developments and potential clinical applications. *Phys. Med.* **32**, 1801–1812. (doi:10.1016/j.ejmp.2016.11.103)
247. Ando M, Sugiyama H, Kunisada T, Shimao D, Takeda K, Hashizume H, Inoue H. 2004 Construction of X-ray dark-field imaging with a view size of 80 mm square and first visualization of human articular cartilage of femoral head under a nearly clinical condition. *Jpn. J. Appl. Phys., Part 2: Lett.* **43**, L1175–L1177. (doi:10.1143/JJAP.43.L1175)
248. Shimao D, Mori K, Sugiyama H, Hyodo K. 2003 Imaging of ligament and articular cartilage due to refraction-contrast using a Laue geometry analyzer crystal. *Jpn. J. Appl. Phys., Part 1: Regul. Pap. Short Notes Rev. Pap.* **42**, 5874–5875. (doi:10.1143/jjap.42.5874)
249. Shimao D *et al.* 2005 X-ray dark-field imaging and potential of its clinical application. In *Medical imaging 2005: physics of medical imaging, Pts 1 and 2*, vol. 5745, pp. 32–39. Japan: Grad. Univ. Adv. Studies, Tsukuba, Ibaraki 305. (doi:10.1117/12.595021)
250. Shimao D, Sugiyama H, Hyodo K, Kunisada T, Ando M. 2005b Evaluation of X-ray dark-field imaging in visualization of nearly clinical articular cartilage. *Nucl. Instrum. Methods Phys. Res. A* **548**, 129–134. (doi:10.1016/j.nima.2005.03.079)
251. Shimao D, Sugiyama H, Kunisada T, Ando M. 2006 Articular cartilage depicted at optimized angular position of Laue angular analyzer by X-ray dark-field imaging. *Appl. Radiat. Isot.* **64**, 868–874. (doi:10.1016/j.apradiso.2006.03.004)
252. Esposito M, Buchanan I, Massimi L, Ferrara J, Shearing P, Olivo A, Endrizzi M. 2023 Laboratory-based X-ray dark-field microscopy. *Phys. Rev. Appl.* **20**, 064039. (doi:10.1103/PhysRevApplied.20.064039)
253. Esposito M, Astolfo A, Cipiccia S, Jones C, Savvidis S, Ferrara J, Endrizzi M, Dudhia J, Olivo A. 2023 Technical note: cartilage imaging with sub-cellular resolution using a laboratory-based phase-contrast X-ray microscope. *Med. Phys.* **50**, 6130–6136. (doi:10.1002/mp.16599)
254. Shimao D, Kunisada T, Sugiyama H, Ando M. 2007 Refraction-enhanced tomosynthesis of a finger joint by X-ray dark-field imaging. *Jpn. J. Appl. Phys., Part 2: Lett.* **46**, L608–L610. (doi:10.1143/JJAP.46.L608)
255. Vittoria FA, Kallon GKN, Basta D, Diemoz PC, Robinson IK, Olivo A, Endrizzi M. 2015 Beam tracking approach for single–shot retrieval of absorption, refraction, and dark–field signals with laboratory X-ray sources. *Appl. Phys. Lett.* **106**, 224102. (doi:10.1063/1.4922189)
256. Bay BK. 1995 Texture correlation: a method for the measurement of detailed strain distributions within trabecular bone. *J. Orthop. Res.* **13**, 258–267. (doi:10.1002/jor.1100130214)
257. Karali A, Kao AP, Zekonyte J, Blunn G, Tozzi G. 2021 Micromechanical evaluation of cortical bone using in situ XCT indentation and digital volume correlation. *J. Mech. Behav. Biomed. Mater.* **115**, 104298. (doi:10.1016/j.jmbbm.2020.104298)
258. Costa MC, Tozzi G, Cristofolini L, Danesi V, Viceconti M, Dall'Ara E. 2017 Micro finite element models of the vertebral body: validation of local displacement predictions. *PLoS ONE* **12**, e0180151. (doi:10.1371/journal.pone.0180151)
259. Disney C, Eckersley A, McConnell J, Geng H, Bodey A, Hoyland J, Lee P, Sherratt M, Bay B. 2019 Synchrotron tomography of intervertebral disc deformation quantified by digital volume correlation reveals microstructural influence on strain patterns. *Acta Biomater.* **92**, 290–304. (doi:10.1016/j.actbio.2019.05.021)
260. Pierantoni M, Sharma K, Kok J, Novak V, Eliasson P, Isaksson H. 2025 Quantification of 3D microstructures in Achilles tendons during *in situ* loading reveals anisotropic fiber response. *Acta Biomater.* **194**, 246–257. (doi:10.1016/j.actbio.2025.01.023)
261. Bay BK, Smith TS, Fyhrie DP, Saad M. 1999 Digital volume correlation: three-dimensional strain mapping using X-ray tomography. *Exp. Mech.* **39**, 217–226. (doi:10.1007/BF02323555)
262. Turunen M, Töyräs J, Lammi M, Jurvelin J, Korhonen R. 2012 Hyperosmolaric contrast agents in cartilage tomography may expose cartilage to overload-induced cell death. *J. Biomech.* **45**, 497–503. (doi:10.1016/j.jbiomech.2011.11.049)
263. Pouran B, Arbabi V, Zadpoor AA, Weinans H. 2016 Isolated effects of external bath osmolality, solute concentration, and electrical charge on solute transport across articular cartilage. *Med. Eng. Phys.* **38**, 1399–1407. (doi:10.1016/j.medengphy.2016.09.003)
264. Zimmerman BK, Nims RJ, Chen A, Hung CT, Ateshian GA. 2021 Direct osmotic pressure measurements in articular cartilage demonstrate nonideal and concentration-dependent phenomena. *J. Biomech. Eng.* **143**, 041007. (doi:10.1115/1.4049158)

265. Paternò G, Cardarelli P, Gambaccini M, Taibi A. 2020 Dual-energy X-ray medical imaging with inverse compton sources: a simulation study. *Crystals* **10**, 834. (doi:10.3390/cryst10090834)
266. Procz S, Avila C, Fey J, Roque G, Schuetz M, Hamann E. 2019 X-ray and gamma imaging with Medipix and Timepix detectors in medical research. *Radiat. Meas.* **127**, 106104. (doi:10.1016/j.radmeas.2019.04.007)
267. Ramilli M *et al.* 2017 Measurements with MÖNCH, a 25 μm pixel pitch hybrid pixel detector. *J. Instrum.* **12**, C01071. (doi:10.1088/1748-0221/12/01/C01071)
268. Munro PR, Rigon L, Ignatyev K, Lopez FC, Dreossi D, Speller RD, Olivo A. 2013 A quantitative, non-interferometric X-ray phase contrast imaging technique. *Opt. Express* **21**, 647. (doi:10.1364/OE.21.000647)
269. Cicek E. 2016 Effect of X-ray irradiation on articular cartilage mechanical properties. *Acta Phys. Pol., A* **129**, 200–202. (doi:10.12693/APhysPolA.129.200)
270. Pe na Fernández M, Cipiccia S, Dall'Ara E, Bodey AJ, Parwani R, Pani M, Blunn GW, Barber AH, Tozzi G. 2018 Effect of SR-microCT radiation on the mechanical integrity of trabecular bone using in situ mechanical testing and digital volume correlation. *J. Mech. Behav. Biomed. Mater.* **88**, 109–119. (doi:10.1016/j.jmbbm.2018.08.012)
271. Barth HD, Zimmermann EA, Schaible E, Tang SY, Alliston T, Ritchie RO. 2011 Characterization of the effects of x-ray irradiation on the hierarchical structure and mechanical properties of human cortical bone. *Biomaterials* **32**, 8892–8904. (doi:10.1016/j.biomaterials.2011.08.013)
272. Willer K *et al.* 2021 X-ray dark-field chest imaging for detection and quantification of emphysema in patients with chronic obstructive pulmonary disease: a diagnostic accuracy study. *Lancet Digit. Health* **3**, e733–e744. (doi:10.1016/S2589-7500(21)00146-1)
273. Gassert FT *et al.* 2021 X-ray dark-field chest imaging: qualitative and quantitative results in healthy humans. *Radiology* **301**, 389–395. (doi:10.1148/radiol.2021210963)
274. Fantoni S, Brombal L, Cardarelli P, Baruffaldi F 2025 Data from: Advanced X-ray techniques for research-oriented high-resolution imaging of articular cartilage: a scoping review. Figshare. (doi:10.6084/m9.figshare.c.8174359)